MAGNETISM OF TRANSITION METAL NANOWIRES

A THESIS

SUBMITTED TO THE DEPARTMENT OF DEPARTMENT OF PHYSICS

AND THE INSTITUTE OF ENGINEERING AND SCIENCE

OF BILKENT UNIVERSITY

IN PARTIAL FULFILLMENT OF THE REQUIREMENTS

FOR THE DEGREE OF

MASTER OF SCIENCE

By

Can ATACA

July, 2008

I certify that I have read this thesis and that in my opinion it is fully adequate, in scope and in quality, as a thesis for the degree of Master of Science.

Prof. Dr. Salim Çıracı (Advisor)

I certify that I have read this thesis and that in my opinion it is fully adequate, in scope and in quality, as a thesis for the degree of Master of Science.

Prof. Dr. Atilla Erçelebi

I certify that I have read this thesis and that in my opinion it is fully adequate, in scope and in quality, as a thesis for the degree of Master of Science.

Assoc. Prof. Dr. Ulrike Salzner

Approved for the Institute of Engineering and Science:

Prof. Dr. Mehmet B. Baray
Director of the Institute Engineering and Science

ABSTRACT

MAGNETISM OF TRANSITION METAL NANOWIRES

Can ATACA

M.S. in Department of Physics

Supervisor: Prof. Dr. Salim Çıracı

July, 2008

In this thesis we investigated structural, electronic and magnetic properties of *3d* (light) transition metal (TM) atomic chains and Cr nanowires using first-principles pseudopotential plane wave calculations. Infinite periodic linear, dimerized linear and planar zigzag chain structures, as well as their short segments consisting of finite number of atoms and chromium nanowires have been considered. For most of the infinite periodic chains, neither linear nor dimerized linear structures are favored; to lower their energy the chains undergo a structural transformation to form planar zigzag and dimerized zigzag geometries. Dimerization in both infinite and finite chains are much stronger than the usual Peierls distortion and appear to depend on the number of *3d*-electrons. As a result of dimerization, a significant energy lowering occurs which, in turn, influences the stability and physical properties. Metallic linear chain of vanadium becomes half-metallic upon dimerization. Infinite linear chain of scandium also becomes half-metallic upon transformation to the zigzag structure. The end effects influence the geometry, energetics and the magnetic ground state of the finite chains. Structure optimization performed using noncollinear approximation indicates significant differences from the collinear approximation. Variation of the cohesive energy of infinite and finite-size chains with respect to the number of *3d*-electrons are found to mimic the bulk behavior pointed out by Friedel.

Furthermore, we considered Cr nanowires, which have cross section comprising a few (4,5 - 9,12) atoms. Chromium nanowires are found to be in a local minimum in the Born-Oppenheimer surface and are ferrimagnetic metals. The type of coupling, as for ferromagnetic or antiferromagnetic, between neighboring Cr atoms depends on their interatomic distances. The spin-orbit coupling of finite chains are found to be negligibly small for finite molecules and Cr nanowires.

ÖZET

GEÇİŞ METALİ NANOTELLERİN MANYETİZMASI

Can ATACA

Fizik Bolumu , Yüksek Lisans

Tez Yöneticisi: Prof. Dr. Salim Çıracı

Temmuz, 2008

Bu tezde, *3d* (hafif) geçiş metali atom zincirlerinin ve krom (Cr) nanotellerin elektronik ve manyetik özelliklerini temel prensipler yalancı potansiyel düzlem dalga hesaplamalarını kullanarak inceledik. Periyodik sonsuz doğrusal, dimerleşmiş doğrusal, düzlemsel doğrusal yapılar; geçiş elementlerinin sonlu sayısıda atomundan oluşan küçük parçacıkları ve krom nanoteller göz önüne alındı. Çoğu periyodik sonsuz zincirler ne doğrusal nede dimerleşmiş doğrusal yapılar enerji olarak uygun değildir; zincirler enerjilerini düşürmek için yapısal değişim geçirerek zigzag veya dimerleşmiş zigzag yapılarına dönüşürler. Sonlu ve sonsuz yapılarda olan dimerleşme alışılmış Peierls bozulmasından daha kuvvetlidir ve hesaplandığına göre *3d* orbitallerindeki elekron sayısına bağlıdır. Dimerleşmenin sonucu olarak, önemli ölçüde enerji azalması olur ve bu yapının karalılığını ve fiziksel özelliklerini etkiler. Metalik doğrusal vanadyum zincirleri dimerleşme sonucu yarı-metal özellikler kazanmıştır. Sonsuz doğrusal skandiyum zincirleri de zigzag yapısına dönüşerek yarı-metal özelliği kazanmaktadır. Uç etkileri sonlu zincirlerin geometrisini, bağlanma enerjisini ve manyetik taban halini etkilemektedir. Eş doğrusal olmayan manyetik yaklaşımla yapılan yapısal optimizasyonlar doğrusal olan manyetik yaklaşımla kayda değer değişiklikler göstermektedir. Sonlu ve sonsuz zincirlerinin bağlanma enerjilerinin *3d* elektron sayıları ile değişmeleri kristal yapısında Friedel tarafından gösterilmiş bağlantıya çok benzemektedir.

Bu tezde *3d* geçiş metali zincirlerden başka değişik kesit alanlarına sahip az sayıda atomdan (4,5 - 9,12) oluşan Cr nanotelleri de inceledik. Çalışılan krom nanoteller Born-Oppenheimer yüzeyinde yerel minimumda bulunmaktadır ve ferrimanyetik metaldir. Komşu Cr atomları arasındaki manyetik etkileşim, antiferromanyetik veya ferromanyetik, atomlar arasındaki uzaklığa bağlıdır. Spin-orbit etkileşmesi sonlu zincirler ve Cr nanoteller için çok küçük olduğu incelenmiştir.

Anahtar sözcükler: ab initio, temel prensipler, yoğunluk fonksiyonel teorisi, geçiş

metali, tek atomlu zincirler, nanoteller, geçiş metali molekülleri.

Acknowledgement

This thesis would not appear in its present form without the kind support of my supervisor Prof. Dr. Salim Çıracı. I would like to thank him for his commitment to helping see this thesis through to its final copy and his equally generous and wise guidance during its development. I am also grateful to him for giving me a chance to complete my Master in less than ten months. I am and will be proud of working in his group all through my life.

I would like to thank to Haldun Sevinçli, Ethem Aktürk, Engin Durgun, Mehmet Topsakal, Erman Bekaroğlu and Seymur Cahangirov for their friendship and advises.

Finally, I am forever indebted to my family for their understanding, endless patience and encouragement whenever I needed.

Contents

List of Figures

List of Tables

Chapter 1

Introduction

It is a classical convention that a magnet would preserve its magnetic properties as it is chopped down to smaller pieces. However one cannot continue chopping forever since there is an atomic limit to that. So what happens to magnetic properties at the atomic and molecular level is an active research area, results of which would open new doors to manufacture several devices in several areas. At atomic level, properties of magnetic materials are results of both intrinsic properties of materials and the interactions between nanoscale molecules. Intrinsic properties may differ from ionic compounds to the bulk metals. At macroscopic level, ferromagnetic metals like Fe, Ni, and Co has varying magnetic moments and total magnetic moment is determined by the difference of majority and minority spin states which are all indicated in a band structure of any given system. Near surfaces of magnetic particle the magnetic moment per atom can change very rapidly, hence this produces larger local magnetic moments than that of the bulk structure of the material where translational symmetry is the most effective component for determination of the ground state electronic and magnetic properties. For ionic compounds, the system is characterized by spatially localized valance electrons and thus is not affected by the distance from the surface. However, for ionic compounds, exchange interactions due to incomplete coordination shell near surface, spin configurations may become disordered and reduce the average net magnetic moment. However, this disorientation can be altered by soe processes

which gives rise to several technological applications as magnetic storage.[1] The scientific research in nanomagnetism can be framed quite concisely. The goal is to (i) create, (ii) explore, and (iii) understand new nanomagnetic materials and phenomena.

1.1 *3d* Transition Metal Monatomic Chains and Chromium Nanowires: Novel, Promising Nanomagnets and Spintronic Devices

Fabrication of nanoscale structures, such as quantum dots, nanowires, atomic chains and functionalized molecules have made a great impact in various fields of science and technology.[2, 3, 4, 5] Size and dimensionality have been shown to strongly affect the physical and chemical properties of matter.[6] Electrons in lower dimensionality undergo a quantization which is different from that in the bulk materials.[7, 8, 9] In nanostructures, the quantum effects, in particular the discrete nature of electronic energies with significant level spacing become pronounced.

Suspended monatomic chains being an ultimate one-dimensional (1D) nanowire have been produced and their fundamental properties have been investigated both theoretically and experimentally.[9, 10, 11, 12, 13, 14, 15, 16, 17, 18, 19, 20] Ballistic electron transport[7] with quantized conductance at room temperature has been observed in metallic nanowires.[10, 16] Moreover, magnetic and transport properties become strongly dependent on the details of atomic configuration. Depending on the type and position of a foreign atom or molecule that is adsorbed on a nanostructure, dramatic changes can occur in the physical properties.[4] Some experimental studies, however, aimed at producing the atomic chains on a substrate.[21] Here the substrate-chain interaction can enter as a new degree of freedom to influence the physical properties.

Unlike the metal and semiconductor atomic chains, not many theoretical studies are performed on transition metal[22, 23, 24, 25] (TM) monatomic chains and nanowires. TM monatomic chains have the ability to be magnetized much easier than the bulk.[26] Large exchange interactions of TM atoms in the bulk are overcome by the large electron kinetic energies, which result in a nonmagnetic ground state with large bandwidth. On the other hand, geometries which are nonmagnetic in bulk may have magnetic ground states in monatomic chains.[26] In addition, it is predicted that the quantum confinement of electrons in metallic chains should result in a magnetic ground state and even in a super paramagnetic state for some of the TM chains[27] at finite temperatures. The central issue here is the stability of the chain and the interplay between 1D geometry and the magnetic ground state.[22, 25]

1.2   Motivation

From the technological point of view, TM monatomic chains and nanowires are important in the spin dependent electronics, namely spintronics.[28] While most of the conventional electronics is based on the transport of information through charges, future generation spintronic devices will take the advantage of the electron spin to double the capacity of electronics. It has been revealed that TM atomic chains and nanowires either suspended or adsorbed on a 1D substrate, such as carbon nanotubes or Si nanowires, can exhibit high spin-polarity or half-metallic behavior relevant the for the spin-valve effect.[4] Recently, first-principles pseudopotential calculations have predicted that the finite-size segments of linear carbon chains capped by specific *3d*-TM atoms display an interesting even-odd disparity depending on the number of carbon atoms.[29] For example, CoC_nCo linear chain has an antiferromagnetic ground state for even n, but the ground state changes to ferromagnetic for odd n. Even more interesting is the ferromagnetic excited state of an antiferromagnetic ground state can operate as a spin-valve when CoC_nCo chain is connected to metallic electrodes from both ends.[29]

As the length of the chain decreases, finite-size effects dominate the magnetic and electronic properties.[1, 22] When compared with the infinite case, the finite-size monatomic chains are less stable to thermal fluctuations.[30] Additional effects on the behavior of nanoparticle are their intrinsic properties and the interaction between them.[1, 30, 31, 32] Effects of noncollinear magnetism have to be taken into account as well.[33, 34, 35] The end atoms also exhibit different behavior with respect to the atoms close to the middle of the structure.[36] Not only the spin dependent electronic properties of TM monatomic chains or nanowires, there are potential applications as nanomagnets in imaging and storage technologies which have also been the forms of interest.

Despite all interesting physical properties of TM atomic chains and nanowires, there is not much known about their atomic and electronic structures, and magnetic properties. In this thesis we achieved better understanding of these chain structures by performing first-principles calculations for investigation of atomic, electronic and magnetic properties.

1.3   Organization of the Thesis

The thesis is organized as follows: Chapter 2 summarizes the theoretical background and approximation methods used through out the study. In Chapter 3 and 4, our studies and results about *3d* transition metal monatomic chains and chromium nanowires are indicated. And finally in Chapter 5, a brief conclusion summaries the result of our studies and suggests possible future works.

Chapter 2

Theoretical Background

2.1 Quantum Theory of Molecular Magnetism

The interaction between the localized single particle magnetic moments for the majority of these molecules can be described by Heisenberg model with isotropic (nearest neighbor) interaction and additional anisotropy term. Antiferromagnetic interaction also have a strong effect on the energy and the state of the system. As a result Heisenberg Hamiltonian will be:

$$H = H_{Heisenberg} + H_{anisotropy} + H_{Zeeman} \tag{2.1}$$

$$H_{Heisenberg} = -\sum_{u,v} J_{uv}\overrightarrow{s}(u) \cdot \overrightarrow{s}(v) \tag{2.2}$$

$$H_{anisotropy} = -\sum_{u=1}^{N} d_u(\overrightarrow{e}(u) \cdot \overrightarrow{s}(u))^2 \tag{2.3}$$

$$H_{Zeeman} = g\mu_B \overrightarrow{B} \cdot \overrightarrow{S} \tag{2.4}$$

J_{uv} is a symmetric matrix containing the exchange parameters between spins at sites u and v. J is $'-'$ for antiferromagnetic coupling and $'+'$ for ferromagnetic coupling. The summation is taken all over all possible sites. The anisotropy term can be simplified for the specific geometry and atoms. Zeeman term in the full Hamiltonian describes the interaction with the external magnetic field. G value,

the direction of the field can be assumed to be in $z-$ direction which simplifies the Hamiltonian. This Hamiltonian usually cannot be solved due to the huge dimensions of the matrix. For single-spin Hamiltonian the anisotropy and the Zeeman Hamiltonians in order will be:

$$H = -D_2 S_z^2 - D_4 S_z^4 + H' \tag{2.5}$$

$$H' = g\mu_B B_x S_x \tag{2.6}$$

In general symmetry plays an important role in calculating eigenvectors and eigenvalues of the given Hamiltonian. The computational power decreases as the symmetry of the system increases. We have to determine the dimension of the Hamiltonian. If there is no symmetry in the system, the dimension of the Hamiltonian for a spin array of N spins with different quantum numbers will be:

$$dim(H) = \prod_{u=1}^{N} (2s(u) + 1) \tag{2.7}$$

To divide the Hilbert space into orthogonal subspaces $H(M)$, the Hamiltonian must commute with S_z which results in M to be a good quantum number.

$$dim(H) = \bigoplus_{M=-S_{max}}^{+S_{max}} , \quad S_{max} = \sum_{u=1}^{N} s(u) \tag{2.8}$$

For any given M, N and $s(u)$, the dimension of the system can be calculated as the number of the product states where $\sum_u = m_u = M$ The solution of this problem after simplifications will be:

$$dim(H(M)) = \frac{1}{(S_{max} - M)!}[(\frac{d}{dz})^{S_{max}-M} \prod_{z=1}^{N} \frac{1 - z^{2s(x)+1}}{1 - z}]_{z=0} \tag{2.9}$$

For the case where all of the spins are equal (s), the maximum total spin quantum number is $S_{max} = Ns$, so the result simplify to:

$$dim(H(M)) = f(N, 2s + 1, S_{max} - M) \, where \tag{2.10}$$

$$f(N, \mu, v) = \sum_{n=0}^{v/\mu} (-1)^n \begin{pmatrix} N \\ n \end{pmatrix} \begin{pmatrix} N - 1 + v - n\mu \\ N - 1 \end{pmatrix} \tag{2.11}$$

The dimensions of the Hamiltonian does not change when M is either $'+'$ or $'-'$. The above equation is also known as a result of de Moivre equation.

If the Hamiltonian commutes with S^2 and all of the individual spins are identical to the dimensions of the orthogonal eigenspace, $H(S, M)$ can also be determined from these. Raising and lowering operator can then be defined as:

$$S^{\pm} = S_x \pm iS_y \tag{2.12}$$

For $0 < M < S_{max}$ one dimensional $H(M)$ can be decomposed into orthogonal subspaces with

$$H(M) = H(M, M) \bigoplus S^- H(M + 1) \tag{2.13}$$

$$S^- H(M + 1) = \bigoplus_{S \geq M+1} H(S, M)$$

It is also instructive to mention the translational symmetry found in spin rings. Defining the cyclic shift operator T defined by its action on the product basis as:

$$T \mid m_1, ..., m_{N-1}, m_N >= \mid m_N, m_1, ..., m_{N-1} > \tag{2.14}$$

And the eigenvalues are given as:

$$z_k = exp\{-i\frac{2\pi k}{N}\}, \quad k = 0, ..., N-1, \quad p_k = 2\pi k/N \qquad (2.15)$$

Here k is named as translational quantum number and p_k as momentum quantum number or crystal momentum. T commutes with both the Hamiltonian and the total spin. As a result of this, any Hamiltonian can be decomposed into simultaneous eigenspaces of S^2, S_z and T.

If the dimension of the system is small enough, the Hamiltonian matrices can be diagonalized exactly with any analytical or numerical method. For higher dimensional systems, one has to use computational resources with some different approximations. One of the simplest methods is the projection method which depends on the multiple application of the Hamiltonian. Another method which depends on partially diagonalization of the matrix is given by Cornelius Lanczos. The method also uses random initial vector which is used for generating orthonormal system where representation of the operator is tridiagonal. Each iteration increases the number of both column and row of the matrix by one. With growing size of the matrix eigenvalues converge to true values of Hamilton matrix.When one wants to make calculations on linear and linear finite structures, DMRG method will result in the most trustable results. Mapping a higher dimensional system to a linear one is another way of using DMRG method in higher dimensional systems. The labeling of atomic sites plays an important role because only nearest neighbor interactions are taken into account. For further information on these methods, one must refer to [37].

To finalize this section, we want to point out the evaluation of thermodynamic observables as a function of temperature T and the magnetic field B. In calculations we will assume that $[H, S_z] = 0$ commutes with each other. The energy dependence of eigenvalues of S_z on B is supplied from the Zeeman term. Defining the partition function as:

$$Z(T, B) = tr\{e^{-\beta H}\} = \sum_v e^{\beta E_v(B)} \qquad (2.16)$$

The magnetization and the susceptibility per molecule are calculated from S_z

as:

$$M(T, B) = -\frac{1}{z}tr\{g\mu_B S_z e^{\beta H}\} \tag{2.17}$$

$$= -\frac{g\mu_B}{Z}\sum_v M_v e^{-\beta E_v(B)} \tag{2.18}$$

$$\chi(T, B) = \frac{\partial M(T, B)}{\partial B} \tag{2.19}$$

$$= \frac{(g\mu_B)^2}{k_B T}\{\frac{1}{Z}\sum_v M_v^2 e^{-\beta E_v(B)} - (\frac{1}{z}\sum_v M_v e^{-\beta E_v(B)})^2\} \tag{2.20}$$

Similarly internal energy and the specific heat are calculated from the Hamiltonian as:

$$U(T, B) = -\frac{1}{z}tr\{He^{-\beta H}\} \tag{2.21}$$

$$= -\frac{1}{Z}\sum_v E_v(B)e^{-\beta E_v(B)} \tag{2.22}$$

$$C(T, B) = \frac{\partial U(T, B)}{\partial B} \tag{2.23}$$

$$= \frac{1}{k_B T^2}\{\frac{1}{Z}\sum_v (E_v(B))^2 e^{-\beta E_v(B)} - (\frac{1}{z}\sum_v E_v(B)e^{-\beta E_v(B)})^2\} \tag{2.24}$$

2.2 Density Functional Theory

Nearly most of the physical properties are related with the total energy or the differences between the total energies of the system. After the invention of the Quantum Mechanic (QM) Theory, we begin to have the ability to describe the events in atomic scales. In early times, modeling and calculations in QM were so hard and lengthy that physicians, chemists, etc. prefer experiments instead of calculations. As the time passed more accurate theories have been invented and computer power increases such that 'The boundary of feasible quantum mechanical calculations has shifted significantly, to the extent that it may now be more cost effective to employ quantum mechanical modeling even when experiments do offer and alternative. Physicists have developed many methods can be used to calculate a wide range of physical properties of materials, such as lattice constants and elastic constants. These methods, which require only a specification

of the ions present (by their atomic number), are usually referred to as ab initio methods.[38]

Until now there are many different ab initio methods which can result accurate answers for tens of atom. Of all of the methods, the total-energy pseudopotential method, stands alone because of the fact that it can handle better number of atoms in calculations. The increase in the number of atoms that can be handled is directly due to an increase in computational efficiency of the ab initio pseudopotential method in reality, which also means that there is an increasing class of problems for which it is more cost effective to use quantum-mechanical modeling than experiments to determine the physical parameters. One can easily see that the cost effectiveness of quantum-mechanical modeling methods over physical experimentation will continue to increase with time.

2.2.1   Total Energy Pseudopotential Calculations

2.2.1.1   Overview of Approximations

To determine the various electronic and geometric structure of a solid requires calculations of QM total energy of the system and subsequent minimization of that energy with respect to electronic and nuclear coordinates. Because of the large mass differences between the nucleus and electrons, electrons will respond to the same forces much faster than the nucleus. We can treat nuclei adiabatically meaning that we separate the nuclear and electronic coordinates in the many-body wave function. This is also known as "Born-Oppenheimer approximation".

The total energy calculations then include density functional theory to model the electron-electron interaction, pseudopotential theory to model the electron-ion interactions, supercells to model systems with periodic geometries and iterative minimization techniques to relax the electronic coordinates.

2.2.1.2   Electron-Electron Interaction

In DFT we assume that instead of solving strongly interacting electron gas, we modeled it as a single particle moving in an effective nonlocal potential. In many electron system, the wave function has to be antisymmetric under the exchange of any two electrons because electrons are fermions. Having the wave function antisymmetric results in spatial separation between electrons that have the same spin and as a result reduces the Coulomb energy of the electronic system. This process which reduces the total energy is known as exchange energy. If electrons that have opposite spins are also spatially separated, the Coulomb energy of the total system can also be reduced below its Hartree-Fock value. The Coulomb energy of the system is reduced, but the kinetic energy of electrons did increased. The difference in energy between the results obtained from Hartree-Fock approximation and the many-body energy of an electronic system is known as correlation energy.

Density Functional Theory is developed by Hohenberg, Kohn and Kohn, Sham for describing the effects of exchange and correlation in an electron gas. Hohenberg and Kohn showed that total energy of an electron gas can be modeled as a unique functional of electron density. Kohn and Sham then showed how to represent the many-electron problem by exactly equivalent set of self consistent one-electron equations.

The Kohn-Sham energy functional for a set of doubly occupied electronic states is given as:

$$E[\psi_i] = 2 \sum_i \int [-\frac{\hbar^2}{2m}]\nabla^2\psi_i d^3r + \int V_{ion}(r)n(r)d^3r + \qquad (2.25)$$

$$\frac{e^2}{2} \int \frac{n(r)n(r^{'})}{\mid r - r^{'} \mid}d^3rd^3r^{'} + E_{XC}[n(r)] + E_{ion}(R_I)$$

E_{ion} is the Coulomb energy provided with interactions among the ions (nucleus) at position R_I, V_{ion} is the total electron-ion potential, $n(r)$ is the electron density and $E_{XC}[n(r)]$ is the exchange-correlation functional.

$$n(r) = 2\sum_i \mid \psi_i(r) \mid^2 \tag{2.26}$$

Determining the set of wave functions ψ_i that gives minimum Kohn-Sham energy functional:

$$\{\frac{-\hbar^2}{2m} \bigtriangledown^2 +V_{ion}(r) + V_H(r) + V_{XC}(r)\}\psi_i(r) = \epsilon_i\psi_i(r) \tag{2.27}$$

Here ψ_i represents the wave function of the ith electronic state and ϵ_i represents the corresponding eigenvalue. $V_H(r)$ is the Hartree potential and $V_{XC}(r)$ is the exchange correlation potential.

$$V_H(r) = e^2 \int \frac{n(r')}{\mid r - r' \mid}d^3r' \tag{2.28}$$

$$V_{XC}(r) = \frac{\delta E_{XC}[n(r)]}{\delta n(r)} \tag{2.29}$$

These equations represent a mapping of the interacting many-electron system to a system of noninteracting electrons in an effective potential caused by all other electrons. We must solve these equations self consistently because the occupied electronic states generate a charge density which will produce the electronic potential which are used in constructing these equations. The Kohn-Sham eigenvalues are not the energies of the single particle electron states, but rather the derivatives of the total energy with respect to the occupation numbers of these states. Nevertheless, the highest occupied eigenvalue in an atomic or molecular calculation is nearly the unrelaxed ionization energy for that system.[39]

The universally used and easiest method used for describing the exchange-correlation energy of an electronic system is local-density approximation (LDA). The main idea behind this approximation is that the exchange-correlation energy of an electronic system is constructed by assuming that the exchange-correlation

energy per electron at a point r n the electron gas, $\epsilon_{XC}(r)$, is equal to the exchange-correlation energy per electron in a homogeneous electron gas that has the same density as the electron at point r.

$$E_{XC}[n(r)] = \int \epsilon_{XC}(r)n(r)d^3r \tag{2.30}$$

$$\frac{\delta E_{XC}[n(r)]}{\delta n(r)} = \frac{\delta[n(r)\epsilon_{XC}(r)]}{\delta n(r)} \tag{2.31}$$

$$\epsilon_{XC}(r) = \epsilon_{XC}^{hom}[n(r)] \tag{2.32}$$

LDA ignores corrections to the exchange-correlation energy at a point r due to nearby inhomogeneities in the electron density. Shortly we can conclude that LDA appears to give a single well-defined global minimum for the energy of a non-spin-polarized system of electrons in a fixed ionic potential. For magnetic material, one has to expect more than one local minimum in energy. The global minimum of the system is then found by monitoring energy functional over a large region of phase space.

2.2.1.3   Periodic Supercells

Up to now I mentioned DFT on small number of atoms. When the system is periodic there are infinitely many number of atoms and electrons. As a result we must include all of the interactions of these particles in our calculations. There are two difficulties of this result. Wave functions must be calculated for each of the infinitely many electrons in the system and the basis set required to expand each wave function is infinite. Here we will use Bloch's Theorem to make life easier.

This theorem states that in a periodic solid each electron wave function can be written as the product of a cell-periodic part and a wavelike part:

$$\psi_i(r) = exp[ik \cdot r]f_i(r) \tag{2.33}$$

Periodic part of the wave function can be expanded using a basis set consisting of a discrete set of plane waves :

$$f_i(r) = \sum_G c_{i,G} exp[iG \cdot r] \tag{2.34}$$

Here reciprocal lattice vectors G are defined by using the fact that $G.l = 2\pi m$. Here l is a lattice vector and m is an integer. Then wave function for each electron can be written as :

$$\psi_i(r) = \sum_G c_{i,k+G} exp[i(k+G) \cdot r] \tag{2.35}$$

By using the boundary conditions electronic states are allowed only at a set of k points in a bulk solid. There is a direct proportionality between the volume of the solid in reciprocal space and the density of allowed k points. By using the Bloch's Theorem we change the problem of calculating infinite number of electronic wave functions to the one of calculating a finite number of electronic wave functions at an infinite number of k points. The electronic wave functions at k points that are very close together will be almost identical and hence it is possible to represent the electronic wave functions over a region of k space by the wave functions at a single k point. In this case the electronic states at only a finite number of k points are required to calculate the electronic potential and hence determine the total energy of the solid. The electronic potential and total energy are more difficult to calculate if the system is metallic because a dense set of k points is required to define the Fermi surface precisely. The magnitude of any error in the total energy due to inadequacy of the k point sampling can always be reduced by using a denser set of k points. The computed total energy will converge as the density of k points increases.[40]

We know that we can expand electronic wave functions at each k point any discrete plane wave basis set by Bloch's Theorem. The coefficients $c_{i,k+G}$ for the

plane waves with small kinetic energy are typically more important those with having a larger energy. By this way we can truncate the plane-wave basis set to include only plane waves that have kinetic energies less than some cutoff energy. Introduction of this cutoff energy to the discrete plane-wave basis set produces a finite basis set. The energy cutoff will lead to small error in total energy calculations, but increasing the value of the cutoff energy, the total energy will converge to a value. By using a denser k point sets we can overcome the problem of discontinuities occurred at different cutoffs for different k points in the k-points set.

Plane-wave representation of Kohn-Sham equations are :

$$\sum_{G'} [\frac{\hbar^2}{2m} \mid k + G \mid^2 \delta_{GG'} + V_{ion}(G - G') +$$

$$V_H(G - G') + V_{XC}(G - G')] c_{i,k+G'} = \epsilon_i c_{i,k+G}$$

(2.36)

The kinetic energy of electrons is diagonal, and the many potentials are described in terms of their Fourier transforms. The dimension of the matrix depends on the cutoff energy value we choose.

2.2.1.4   Electron-Ion Interactions

To perform calculation including the effect of all ions and electrons, an extremely large plane wave basis set would be required and a huge amount of computational time would be required to calculate the electronic wave function. It is well known that most physical properties of solids are dependent on the valance electrons to a much greater extent than the core electrons. The pseudopotential approximation exploits this by removing the core electrons and by replacing them and the strong ionic potential by a weaker pseudopotential that acts on a set of pseudo wave functions rather than the true valance wave function. The valance wave functions oscillate rapidly in the region occupied by the core electrons due to the strong ionic potential in this region. These oscillations maintain the orthogonality between the core wave functions and the valance wave functions, which is required by the exclusion principle. The scattering from the pseudopotential

must be angular momentum dependent because the phase shift introduced by the ion core is different for each angular momentum component of the valance wave function.

$$V_{NL} = \sum_{lm} \mid lm \rangle V_l \langle lm \mid \qquad (2.37)$$

Here $\mid lm >$ represents the spherical harmonics and V_l is the pseudopotential for the angular momentum. A local pseudopotential uses the same potential for all the angular momentum components and its amplitude is only a function of the distance from the nucleus.

We refer to the electron density in the exchange-correlation energy in total energy calculations. If we can find the accurate exchange-correlation energy, we must have the pseudo and real wave function to be identical in both amplitude and spatial dependences. These will result in charge densities to be the same. Nonlocal pseudopotential that uses different potential for different angular momentum values will describe the scattering from the ion core the best. The one to one correspondence between the pseudo and real wave functions outside the core region also proves that the first order energy dependence of the scattering from the ion core is correct, which results in scattering process is accurately described over a wide range of energy.

As we use pseudopotential in our calculation we can use fewer plane wave basis states. By this way we removed the rapid oscillations of the valance wave function in the core region of the atom. Small core region electrons are not present at this time. The total energy of the system is much less than the case of all-electrons, but the difference between the electronic energies of different ionic configurations is very similar to all electron case. We can conclude that the total energy is meaningless until now. The true and the important value are the differences in energies.

2.2.1.5   Ion-Ion Interaction

The Coulomb interaction in real and reciprocal space is long ranged. We have to develop another method for including effects of ion-ion interactions. Using Edwald's method, one can obtain the equation given below.

$$\sum_l \frac{1}{R_1 + l - R_2} = \frac{2}{\sqrt{2}\pi} \sum_l \int_\eta^\infty exp[- \mid R_1 + l - R_2 \mid^2 \rho^2]d\rho + \tag{2.38}$$

$$\frac{2\pi}{\Omega} \sum_G \int_0^\eta exp\{-\frac{\mid G \mid^2}{4\rho^2}\}xexp[i(R_1 - R_2) \cdot G]\frac{1}{\rho^3}d\rho$$

Where l is lattice vectors ad G is reciprocal lattice vectors and Ω is the volume of the unit cell as before. In this method we try to write the lattice summation of the Coulomb energy with respect to the interaction between an ion positioned at R_2 and an array of atoms positioned at $R_2 + l$. This valid for '+' values of the variable η. If we can find an appropriate value for this variable, two summations became rapidly convergent. As a result real and reciprocal space summation can be calculated by few lattice vectors and few reciprocal vectors. For the calculation of the correct energy, we must remove $G = 0$ contribution of the Coulomb energy of the ionic system. Omitting $G = 0$ summation in reciprocal space finally we achieve the relation as :

$$E_{ion} = \frac{1}{2} \sum_{I,J} Z_I Z_J e^2 \{\sum_l \frac{erfc(\eta \mid R_1 + l - R_2 \mid)}{\mid R_1 + l - R_2 \mid} - \frac{2\eta}{\sqrt{2}\rho}\delta_{IJ} + \tag{2.39}$$

$$\frac{4\pi}{\Omega} \sum_{G \neq 0} \frac{1}{\mid G \mid^2} exp\{-\frac{\mid G \mid^2}{4\eta^2}\}cos[(R_1 - R2) \cdot G] - \frac{\pi}{\eta^2\Omega}\}$$

Z is the valances of ions I and J. $erfc$ is the error function. $L = 0$ term is neglected because ion does not interfere with its own charge.

2.2.2 Noncollinear Magnetism

In cases where both AFM and FM couplings occur and compete with each other, collinear magnetism fails for modeling the ground state magnetic ordering. A midway between AFM and FM exchange interactions results in allowing the spin quantization axis to vary in every site of the structure. Geometric structure also influences noncollinear magnetism. Frustrated antiferromagnets having triangular lattice structure, disordered systems as well as broken symmetry on the surface will result in noncollinear magnetism. Spin glasses, α-Mn, domain walls, Fe clusters are typical examples of noncollinearity.

There are many different approaches for implementing noncollinear magnetism, such as ASW (Augmented Spherical Wave), CPA (Coherent-Potential Approximation), LSDA (Local-Spin-Density Approximation). In our study, we use fully unconstrained approach to noncollinear magnetism.[41] In the PAW method the wavefunctions ψ_n^α are derived from the pseudo-wavefunction $\widetilde{\psi_n^\alpha}$ by a linear transformation in which the spin indices are included.

$$\mid \psi_n^\alpha > = \mid \widetilde{\psi_n^\alpha} > + \sum_i (\mid \phi_i > - \mid \widetilde{\phi}_i >) < \widetilde{p}_i \mid \widetilde{\psi_n^\alpha} > \tag{2.40}$$

Index i is used for the atomic site $\mathbf{R}$, $L = l, m$ is the angular moment quantum numbers and k is referring to the reference energy ϵ_{kl}. For noncollinear magnetism, pseudo-wave functions are defined to consist of $2N$ eigenspinors where N is the total number of atoms. Pseudo-wave functions are expended in reciprocal space into plane waves

$$< r \mid \widetilde{\psi_n^\alpha} > = \frac{1}{\Omega_r^{1/2}} \sum_k C_{nk}^\alpha(r) e^{ik/cdotr} \tag{2.41}$$

Where Ω_r is the Wigner-Seitz cell. Partial waves ϕ_i are taken from nonmagnetic reference atom, the pseudo partial waves are equivalent to all electron (AE)

partial waves outside a core radius r_c^l. One can obtain the AE total density matrix starting from 2.40 and is given in 2.42

$$n^{\alpha\beta}(r) = \widetilde{n}^{\alpha\beta}(r) +^1 n^{\alpha\beta}(r) -^1 \widetilde{n}^{\alpha\beta}(r) \tag{2.42}$$

where $\tilde{n}$ is the soft pseudodensity matrix calculated directly from the pseudowave functions on a plane-wave grid. The on-site density matrices ^1n and $^1\widetilde{n}$ are treated on a radial support grid around each atom. For detailed information on these, see [41].

The total energy functional consists of 3 terms. $E = \tilde{E} + E^1 - \tilde{E}^1$. $\tilde{E}$ is the smooth part which is evaluated on regular grids in Fourier or real space. E^1 and $\tilde{E}^1$ are two one-center contributions and indicated in 2.43

$$\tilde{E} = \sum_{\alpha}\sum_{n} f_n < \widetilde{\psi_n^\alpha} \mid -\frac{1}{2}\Delta \mid \widetilde{\psi_n^\alpha} > + E_{XC}[\tilde{n}^{\alpha\beta} + \hat{n}^{\alpha\beta} + \tilde{n}_c] + \tag{2.43}$$

$$E_H[\tilde{n}_{Tr} + \hat{n}_{Tr}] + \int v_H[\tilde{n}_{Zc}](r)[\tilde{n}_{Tr}(r) + \hat{n}_{Tr}(r)]dr + U(R, Z_{ion})$$

$$\tilde{E}^1 = \sum_{\alpha\beta}\sum_{i,j} \rho_{ij}^{\alpha\beta} < \tilde{\phi}_i \mid -\frac{1}{2}\Delta \mid \tilde{\phi}_j + \overline{E_{XC}[^1\tilde{n}^{\alpha\beta} + \hat{n}^{\alpha\beta} + \tilde{n}_c]} + \tag{2.44}$$

$$\overline{E_H[^1\tilde{n}_{Tr} + \hat{n}_{Tr}]} + \int_{\Omega_r} v_H[\tilde{n}_{Zc}](r)[^1\tilde{n}_{Tr}(r) + \hat{n}_{Tr}(r)]dr$$

$$E^1 = \sum_{\alpha\beta}\sum_{i,j} \rho_{ij}^{\alpha\beta} < \phi_i \mid -\frac{1}{2}\Delta \mid \phi_j + \overline{E_{XC}[^1n^{\alpha\beta} + n_c]} + \overline{E_H[^1n_{Tr}]} \tag{2.45}$$

$$+ \int_{\Omega_r} v_H[n_{Zc}](r)^1 n_{Tr}(r)dr$$

where $U(R, Z_{ion})$ is the electrostatic energy of point charges $Z_i on$ in a uniform electrostatic background and pseudized core density $\tilde{n}_{Zc}$ is a charge distribution

that is equivalent to n_{Zc} inside the core region.The Hamiltonian of the system after making simplifications and approximations will be:

$$
\begin{aligned}
H^{\alpha\beta}[n,\{\mathbf{R}\}] \;=\; & -\frac{1}{2}\delta_{\alpha\beta} + \tilde{v}_{\text{eff}}^{\alpha\beta} + \\
& \sum_{(i,j)} |\tilde{p}_i> (\hat{D}_{ij}^{\alpha\beta} +^1 D_{ij}^{\alpha\beta} -^1 \tilde{D}_{ij}^{\alpha\beta}) <\tilde{p}_j|
\end{aligned}
\tag{2.46}
$$

Here $\tilde{v}_{\text{eff}}^{\alpha\beta}$ is the effective one-electron potential which depends on the electron density and the magnetization at each site; $-\frac{1}{2}\delta_{\alpha\beta}$ stands for the kinetic energy of the system. $\hat{D}_{ij}^{\alpha\beta}$, $^1D_{ij}^{\alpha\beta}$ and $^1\tilde{D}_{ij}^{\alpha\beta}$ terms in the summation sign over augmented channels represent the correction terms for long range, effective potential and wave functions. For further details see Ref.[41, 42, 43, 44, 45, 46]

Chapter 3

3d Transition Metal Monatomic Chains

Nowadays size is a significant criterion. Atomic scale storage devices, spin based communication and computation devices, magnetism in linear metallic structures are all a topic of intense interest in today's world. Quantum confinement of the electrons in one or more dimension is a consequence of reducing dimensionality and size of devices. The simplest case is one dimensional transition metal magnetic systems, which foresees a wide range of magnetic phenomena and properties unknown in higher dimensions. Even the fabrication of such structures is challenging, the theoretical explanation is more complicated than the simple crystal structures of these systems.

In this chapter, we consider infinite, periodic chains of *3d*-TM atoms having linear and planar zigzag structures and their short segments consisting of finite number of atoms. For the sake of comparison, Cu and Zn chains are also included in our study. All the chain structures discussed in this paper do not correspond to the global minimum, but may belong to a local minimum. The infinite and periodic geometry is of academic interest and can also be representative for very long monatomic chains. The main interest is, however, in the short segments comprising finite number of TM atoms. We examined the variation of energy as

a function of the lattice constant in different magnetic states, and determined stable infinite and also finite-size chain structures. We investigated the electronic and magnetic properties of these structures. Present study revealed a number of properties of fundamental and technological interest: The linear geometry of the infinite, periodic chain is not stable for most of the *3d*-TM atoms. Even in linear geometry, atoms are dimerized to lower the energy of the chain. We found that infinite linear vanadium chains are metallic, but become half-metallic upon dimerization. The planar zigzag chains are more energetic and correspond to a local minimum. For specific TM chains, the energy can further be lowered through dimer formation within planar zigzag geometry. Dramatic changes in the electronic properties occur as a result of dimerization. The magnetic properties of short monatomic chains have been investigated using both collinear and non-collinear approximation, which are resulted in different net magnetic moment for specific chains. Spin-orbit coupling which is calculated for different initial easy axis of magnetization has been found to be negligibly small.

3.1 Method of calculations

We have performed first-principles plane wave calculations[38, 47] within Density-Functional Theory (DFT)[48] using ultra-soft pseudopotentials.[49] We also used PAW[50] potentials for the noncollinear and noncollinear spin-orbit calculations of the finite chains. The exchange-correlation potential has been approximated by generalized gradient approximation (GGA).[51] For the partial occupancies, we have used the Methfessel-Paxton smearing method.[52] The width of smearing for the infinite structures has been chosen as 0.1 eV for geometry relaxations and as 0.01 eV for the accurate energy band and the density of state (DOS) calculations. As for the finite structures, the width of smearing is taken as 0.01 eV. We treated the chain structures by supercell geometry (with lattice parameters a_{sc}, b_{sc}, and c_{sc}) using the periodic boundary conditions. A large spacing (~ 10 Å) between the adjacent chains has been assured to prevent interactions between them. In single cell calculations of the infinite systems, c_{sc} has been taken to be equal to the lattice constant of the chain. The number of plane waves used in expanding

Bloch functions and **k**-points used in sampling the Brillouin zone (BZ) have been determined by a series of convergence tests. Accordingly, in the self-consistent potential and the total energy calculations the BZ has been sampled by (1x1x41) mesh points in **k**-space within Monkhorst-Pack scheme. [40] A plane-wave basis set with the kinetic energy cutoff $\hbar^2|\mathbf{k} + \mathbf{G}|^2/2m = 350$ eV has been used. In calculations involving PAW potentials, kinetic energy cutoff is taken as $400\ eV$. All the atomic positions and lattice constants (c_{sc}) have been optimized by using the conjugate gradient method where the total energy and the atomic forces are minimized. The convergence is achieved when the difference of the total energies of last two consecutive steps is less than 10^{-5} eV and the maximum force allowed on each atom is 0.05 eV/Å. As for the finite structures, supercell has been constructed in order to assure ~ 10 Ådistance between the atoms of adjacent finite chain in all directions and BZ is sampled only at the Γ-point. The other parameters of the calculations have been kept the same. The total energy of the optimized structure (E_T) relative to free atom energies is negative, if it is in a binding state. As a rule, the structure becomes more energetic (or stable) as its total energy is lowered. Figure 3.1 describes various chain structures of TM atoms treated in this study. These are the infinite periodic chains and the segments of a small number of atoms forming a string or a planar zigzag geometry. The stability of structure-optimized finite chains are further tested by displacing atoms from their equilibrium positions in the plane and subsequently reoptimizing the structure. Finite-size clusters of TM atoms are beyond the scope of this thesis.

3.2 Infinite and Periodic Chain Structures

Figure 3.2 shows the energy versus lattice constant of various infinite and periodic chain structures (described in Fig. 3.1) in different magnetic states. These are the infinite linear (L), the dimerized linear (LD), the planar zigzag (ZZ), and the dimerized zigzag (ZZD) monatomic chains. WZ is a planar zigzag monatomic chain which has apical angle $\alpha > 100^0$. In calculating the ferromagnetic (FM) state, the structure is optimized each time using a spin-polarized GGA calculations starting with a different preset magnetic moment in agreement with Hund's
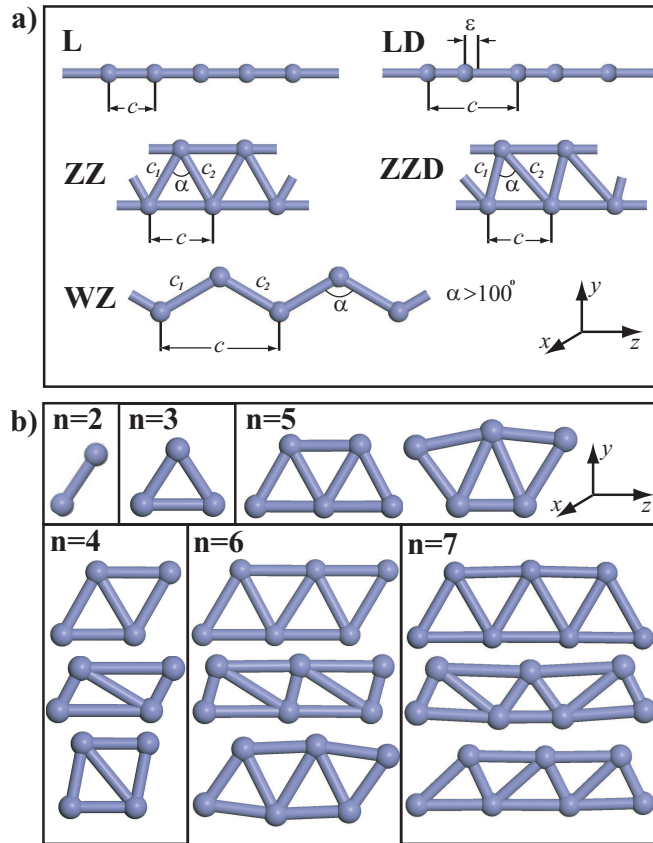
Figure 3.1: Various structures of $3d$-TM atomic chains. (a) Infinite and periodic structures; L: The infinite linear monatomic chain of TM atom with lattice constant, c. LD: The dimerized linear monatomic chain with two TM atoms in the cell. ϵ is the displacement of the second atom from the middle of the unit cell. ZZ: The planar zigzag monatomic chain with lattice parameter c and unit cell having two TM atoms. $c_1 \sim c_2$ and $59^0 < \alpha < 62^0$. ZZD: The dimerized zigzag structure $c_1 \neq c_2$. WZ: The wide angle zigzag structure $c_1 \sim c_2$, but $\alpha > 100^0$. (b) Various chain structures of small segments consisting of finite number (n) of TM atoms, denoted by $(\text{TM})_n$.

rule. The relaxed magnetic moment yielding to the lowest total energy has been
taken as the FM state of the chain. For the antiferromagnetic (AFM) state, we
assigned different initial spins of opposite directions to adjacent atoms and re-
laxed the structure. We performed spin-unpolarized GGA calculations for the
nonmagnetic (NM) state. The energy per unit cell relative to the free constituent
atoms is calculated from the expression, $E = [NE_a - E_T]$, in terms of the to-
tal energy per unit cell of the given chain structure for a given magnetic state
(E_T) and the ground state energy of the free constituent TM atom, E_a. N is
the number of TM atom in the unit cell, that is $N=1$ for L, but $N=2$ for LD,
ZZ, and ZZD structures. The minimum of E is the binding energy. By conven-
tion $E_b < 0$ corresponds to a binding structure, but not necessary to a stable
structure. The cohesive energy per atom is $E_c = -E_b/N$. Light transition metal
atoms can have different structural and magnetic states depending on the number
of their *3d* electrons. For example, Sc having a single *3d* electron, has a shallow
minimum corresponding to a dimerized linear chain structure in the FM state.
If the L structure is dimerized to make a LD structure, the energy of the chain
is slightly lowered. Other linear structures, such as linear NM, and AFM states
have higher energy. More stable structure ZZ is, however, in the FM state. This
situation is rather different for other *3d* TM elements. For example, Cr has LD
and more energetic ZZD structures in the AFM state. It should be noted that in
the dimerized linear chain structure of Cr the displacement of the second atom
from the middle of the unit cell, ϵ, is rather large. Apparently, the dimerization
is stronger than the usual Peierls distortion. As a result, the nearest neighbor
distance, $(c - \epsilon)$, is much smaller than the second nearest neighbor distance,
$(c + \epsilon)$. This situation poses the question whether the interaction between the
adjacent dimers are strong enough to maintain the coherence of the chain struc-
ture. We address this question by comparing the energies of individual dimers
with the chain structure. The formation of the LD structure is energetically more
favorable with respect to individual dimer by 0.54 eV per atom. Furthermore,
the charge accumulation, namely the positive part of the difference between the
charge density of the interacting system and that of the non-interacting system,
presented in Fig. 3.3, indicates a significant bonding between the adjacent dimers.
On the other hand the bonding in a dimer is much stronger than the one in a L

chain. Nevertheless, the LD structure has to transform to more energetic ZZD structure. The zigzag structures in the AFM, FM and NM states have minima at higher binding energies and hence are unstable.

The linear structures of Ti atoms always prefer dimerized geometries and the displacement of the second atom from the middle of the unit cell is large. There is also a remarkable energy difference between L and LD structures in favor of the latter. Energies of LD AFM, FM and NM structures are very close to each other. Looking at the bandstructure of L and LD Ti chain on Fig. 3.7, it can easily be seen that dimerization forms flat bands which are results of localized electrons. This band structure suggests that Ti atoms form two atom molecules which interact weakly with adjacent dimer molecules. However, more energetic ZZ structures do not dimerize. All magnetic structures of V prefer to dimerize. Dimerization of V atoms also influence the magnetic and the electronic properties of the structure. One sees that the number of flat bands increases after dimerization. Vanadium is the only light TM monatomic ZZ chain which appears in the NM lowest energy state. The linear and the linear dimerized Fe chains have a local minimum in the FM state. More stable ZZ and ZZD structures in the FM state have almost identical minima in lower binding energy. The ferromagnetic planar zigzag chain structure appears to be the lowest energy structure for Mn. Both Co and Ni monatomic chains prefer the FM state in both L and ZZ structures. The energy of ZZ chain in the FM state is lowered slightly upon dimerization. The displacement of the second atom in ZZD structure is also not very large. It is also saliency to note that Fe, Mn and Co chains in the NM state undergo a structural transformation from ZZ to WZ structure. As the number of electrons in the d-shell of atom increases, the effect of dimerization on the energy and the geometry of the structure decreases. Therefore it can be concluded that $3d$-TM atoms having fewer electrons can make hybridization easier. It is noted from Fig. 3.2 that the structure of *3d*-TM atomic chains are strongly dependent on their magnetic state. Optimized structural parameters, cohesive energy, magnetic state and net magnetic moment of infinite linear and zigzag structures are presented in Table 4.1 and Table 4.2, respectively.

In Fig. 3.4 and Fig. 3.5 we compare the nearest neighbor distance and the
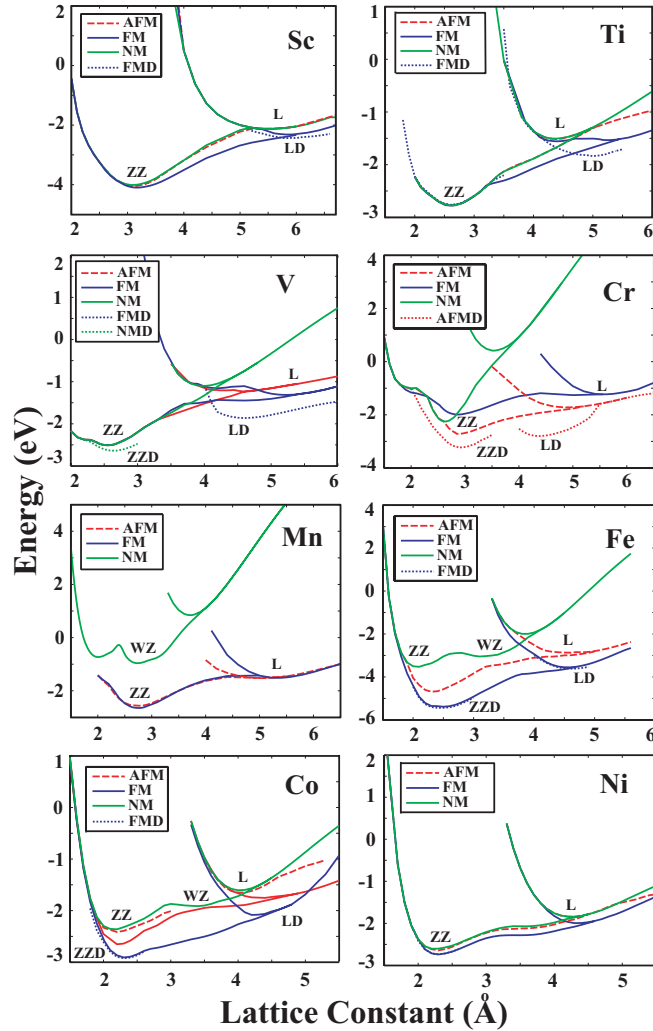
Figure 3.2: The energy versus lattice constant, c, of various chain structures in different magnetic states. FM: ferromagnetic; AFM: antiferromagnetic; NM: non-magnetic; FMD: ferromagnetic state in the linear or zigzag dimerized structure; AFMD: antiferromagnetic state in the dimerized linear or zigzag structure. The energy is taken as the energy per unit cell relative to the free constituent atom energies in their ground state (See text for definition). In order to compare the energy of the L structure with that of the LD, the unit cell (and also lattice constant) of the former is doubled in the plot. Types of structures identified as L, LD, ZZ, ZZD, WZ are describes in Fig. 3.1.

	Sc	Ti	V	Cr	Mn	Fe	Co	Ni	Cu	Zn
c	6.0	4.9	4.5	4.4	2.6	4.6	2.1	2.2	2.3	2.6
ε	0.38	0.52	0.51	0.66	0.0	0.21	0.0	0.0	0.0	0.0
E_c	1.20	1.83	1.86	1.40	0.76	1.81	2.10	1.99	1.54	0.15
MGS	FM	FM	FM	AFM	AFM	FM	FM	FM	NM	NM
μ	1.74	0.45	1.00	±1.95	±4.40	3.32	2.18	1.14	0.0	0.0

Table 3.1: The calculated values for linear structures (L and LD). The lattice constant, c (in Å); the displacement of the second atom in the unit cell of dimerized linear structure, ϵ (in Å); cohesive energy, E_c (in eV/atom); the magnetic ground state, MGS; and the total magnetic moment, μ per unit cell (in Bohr magnetons, μ_B) obtained within collinear approximation.

	Sc	Ti	V	Cr	Mn	Fe	Co	Ni	Cu	Zn
c	3.17	2.60	2.60	2.90	2.76	2.40	2.30	2.30	2.40	2.50
c_1	2.94	2.43	1.84	1.57	2.64	2.24	2.23	2.33	2.39	2.67
c_2	2.94	2.45	2.42	2.65	2.64	2.42	2.39	2.33	2.39	2.67
α	65.2	64.5	73.8	82.6	63.0	61.9	59.6	59.1	60.2	55.8
E_c	2.05	2.78	2.64	1.57	1.32	2.69	2.91	2.74	2.16	0.37
MGS	FM	FM	NM	AFM	FM	FM	FM	FM	NM	NM
μ	0.99	0.18	0.0	±1.82	4.36	3.19	2.05	0.92	0.0	0.0

Table 3.2: The calculated values for the planar zigzag structures (ZZ and ZZD): The lattice constant, c (in Å); the first nearest neighbor, c_1 (in Å); the second nearest neighbor, c_2 (in Å); angle between them, α (in degrees); the cohesive energy, E_c (in eV/atom); the magnetic ground state, MGS; and the total magnetic moment, μ per unit cell (in Bohr magnetons, μ_B) obtained within collinear approximation.

average cohesive energy of the linear and zigzag chain structures with those of the bulk metals and plot their variations with respect to their number of *3d* electrons of the TM atom. The nearest neighbor distance in the linear and zigzag structures are smaller than that of the corresponding bulk structure, but display the similar trend. Namely, it is large for Sc having a single *3d* electron and decreases as the number of *3d* electrons, *i.e.* N_d, increases to four. Mn is an exception, since the bulk and the chain structure show opposite behavior. While the nearest neighbor distance of bulk Mn is a minimum, it attains a maximum value in the chain structure. Owing to their smaller coordination number, chain structures have smaller cohesive energy as compared to the bulk crystals as shown in Fig. 3.5. However, both L (or LD if it has a lower energy) and ZZ (or ZZD if it has a lower energy) also show the well-known double hump behavior which is characteristics of the bulk TM crystals. Earlier, this behavior was explained for the bulk TM crystals.[5, 53, 54] The cohesive energy of zigzag structures are generally ~ 0.7 eV larger than that of the linear structures. However, it is 1-2 eV smaller than that of the bulk crystal. This implies that stable chain structures treated in this study correspond only to a local minima in the Born-Oppenheimer surface.

We note that spin-polarized calculations are carried out under collinear approximation. It is observed that all chain structures presented in Table 4.1 and Table 4.2 have magnetic state if $N_d < 9$. Only Cr and Mn linear chain structures and Cr zigzag chain structure have an AFM lowest energy state. The binding energy difference between the AFM state and the FM state, $\Delta E = E_b^{AFM} - E_b^{FM}$, is calculated for all *3d* TMs. Variation of ΔE with N_d is plotted in Fig. 3.6. We see that only Cr ZZ and ZZD chains have an AFM lowest energy state. ΔE of Fe is positive and has the largest value among all *3d*-TM zigzag chains. Note that ΔE increases significantly as a result of dimerization.

Having discussed the atomic structure of *3d*-TM chains, we next examine their electronic band structure. In Fig. 3.7, the chain structures in the first column do not dimerize. The linear chains placed in the third column are dimerized and changed from the L structure placed in the second column to form the LD structure. Most of the linear structures in Fig. 3.7 display a FM metallic character with
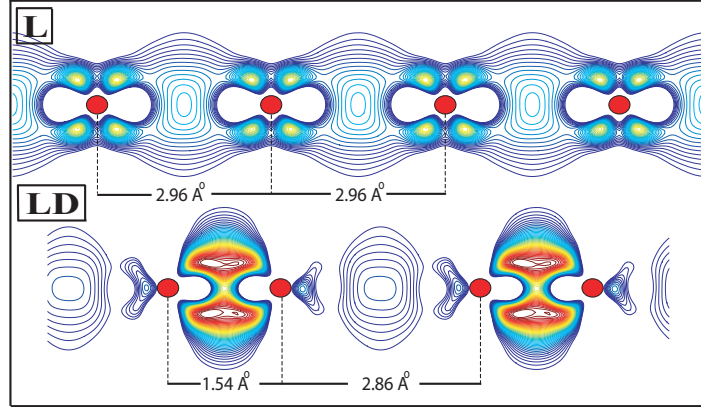
Figure 3.3: The plot of charge accumulation, namely the positive part of the difference between the charge density of the interacting system and that of the non-interacting system, for the linear (L) and the dimerized linear structure (LD) of Cr monatomic chains. Contour spacings are equal to $\Delta\rho = 0.0827e/\text{Å}^3$. The outermost contour corresponds to $\Delta\rho = 0.0827e/\text{Å}^3$. Dark balls indicate Cr atom.
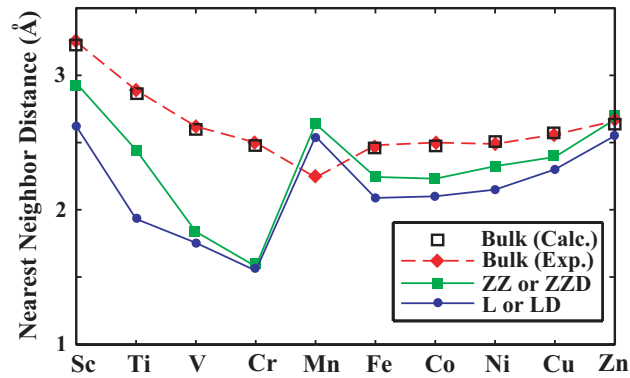
Figure 3.4: Variation of the nearest neighbor distance of $3d$-TM atomic chains and the bulk structures. For the linear and zigzag structures the lowest energy configuration (i.e. symmetric or dimerized one) has been taken into account. Experimental values of the bulk nearest neighbor distances have been taken from Ref.citekittel].
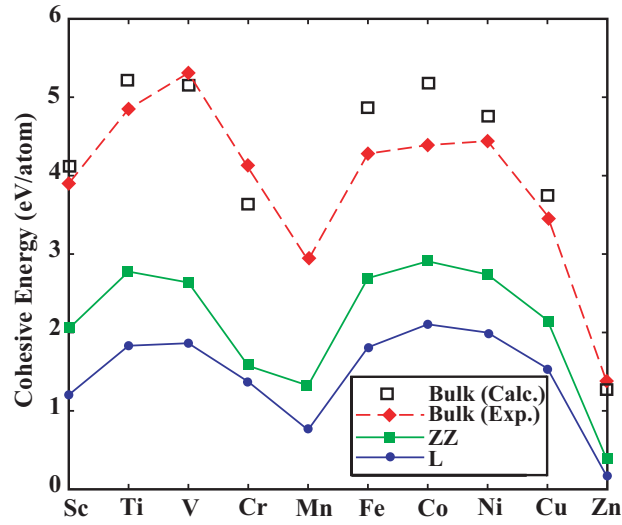
Figure 3.5: Variation of the cohesive energy, E_c (per atom), of *3d*-TM monatomic chains in their lowest energy linear, zigzag and bulk structures. For the linear and zigzag structures the highest cohesive energy configuration (i.e. symmetric or dimerized one) has been taken into account. Experimental values of the bulk cohesive energies have been taken from Ref.[[55]]
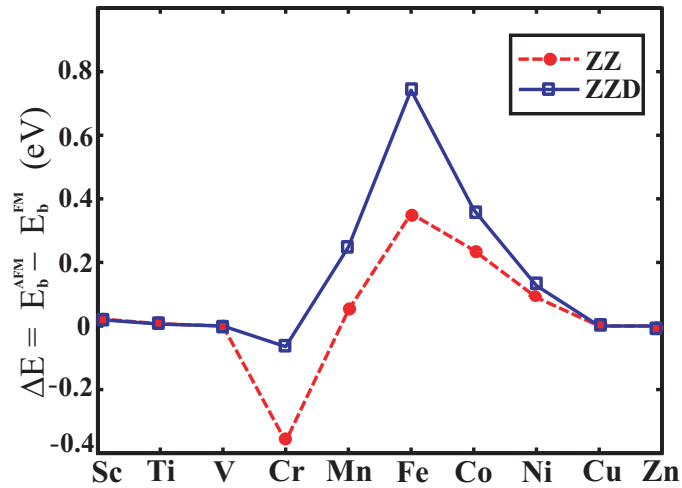
Figure 3.6: Variation of the binding energy difference, ΔE (per atom) between the lowest antiferromagnetic and ferromagnetic states of *3d*-TM monatomic chains. Open squares and filled circles are for the symmetric zigzag ZZ and dimerized zigzag ZZD chains respectively.
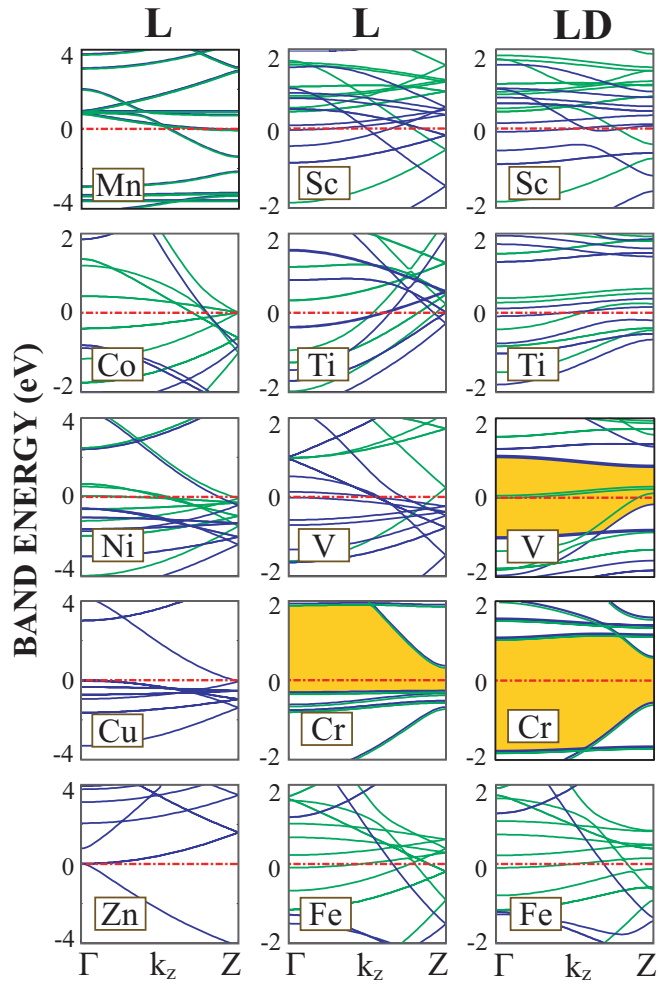
Figure 3.7: Energy band structures of *3d*-TM atomic chains in their L and LD structures. The zero of energy is set at the Fermi level. Gray and black lines are minority and majority bands, respectively. In the antiferromagnetic state majority and minority bands coincide. Energy gaps between the valence and the conduction bands are shaded.

broken spin degeneracy. A few exceptions are Mn, Cr, and V chains. The linear Mn chain has an AFM state, where spin-up (majority) and spin-down (minority) bands coincide. Chromium L and LD structures are AFM semiconductors. Vanadium is a ferromagnetic metal for both spins, but becomes half-metallic upon dimerization. In half-metallic state, the chain has integer number of net spin in the unit cell. Accordingly, Vanadium chain in the LD structure is metallic for one spin direction, but semiconducting for the other spin direction. Hence, the spin polarization at the Fermi level, *i.e.* $P = [D_\uparrow(E_F) - D_\downarrow(E_F)]/[D_\uparrow(E_F) + D_\downarrow(E_F)]$ is 100%. Bands of Cu and Zn with filled *3d*-shell in nonmagnetic state are in agreement with previous calculations.[56] In Fig. 3.8, the chain structures in the first column have only ZZ structure. The zigzag chains in the second column are transformed to a lower energy (*i.e.* more energetic) ZZD structure in the third column. The ZZ chain of Sc is stable in a local minimum and displays a half-metallic character with 100% spin-polarization at the Fermi level. Accordingly, a long segment of ZZ chain of Sc can be used as a spin-valve. Ti, Mn, and Ni in their stable zigzag structures are FM metals. The stable ZZD structure of Fe and Co chains are also FM metals. The ZZ and relatively lower energy ZZD structure of V chain are nonmagnetic. Both ZZ and ZZD structures of Cr are in the AFM state.

For Co and Fe in the ZZD structure more bands of one type of spin cross the Fermi level as compared to those of the other type of spin resulting in a high spin-polarization at the Fermi level. This situation implies that in the ballistic electron transport, the conductance of electrons with one type of spin is superior to electrons with the opposite type of spin; namely $\sigma_\downarrow \gg \sigma_\uparrow$. Accordingly, the conductance of electrons across Fe and Co chains becomes strongly dependent on their spin-directions. This behavior of the infinite periodic Fe or Co chain is expected to be unaltered to some extend for long, but finite chains and can be utilized as a spin-dependent electronic device. In closing this section, we want to emphasize that the infinite, periodic chains of *3d*-TM atoms can be in the zigzag structure corresponding to a local minimum. However, most of the zigzag structures are dimerized. Dimerization causes remarkable changes in electronic and magnetic properties.
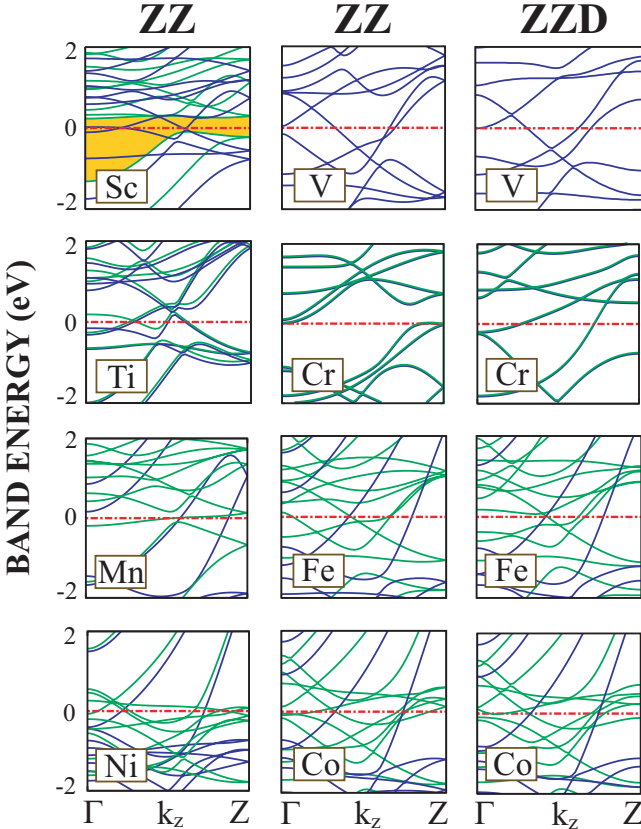
Figure 3.8: Energy band structures of *3d*-TM atomic chains in their zigzag (ZZ) and dimerized zigzag (ZZD) structures. The zero of energy is set at the Fermi level. Gray and black lines are minority and majority spin bands, respectively. The gray and dark lines coincide in the antiferromagnetic state. Only dark lines describe the bands of nonmagnetic state. The energy gap between the valence and the conduction bands is shaded.

3.3   Short Chain Structures

Periodic infinite chains in Section III are only ideal structures; long finite-size segments perhaps can attain their physical properties revealed above. On the other hand, the end effects can be crucial for short segments consisting of few atoms which may be important for various spintronic applications. In this section, we examine short segments of $3d$-TM chains consisting of n atoms, where n=2-7.

3.3.1   Collinear Approximation

We first study the atomic structure and magnetic properties of the finite chains within collinear approximation using ultra-soft pseudopotentials.[49] The linear structure is unstable for the finite-size segments. Various planar zigzag structures, which are only a local minima, are described in Fig. 3.1. We optimized the geometry of these zigzag structures with different initial conditions of magnetic moment on the atoms within collinear approximation. If the final optimized structures for q different initial conditions result in different average cohesive energy (or different total energy), they may actually trapped in different local minima. Here we considered following different initial conditions: (1) At the beginning, opposite magnetic moments, $\pm\mu_a$, have been assigned to adjacent atoms, and the total magnetic moment, $\mu = \sum \mu_a$, has been forced to vanish at the end of optimization for $n = 2-7$. Initial magnetic moment, μ_a, on atoms are determined from the Hund's rule. (2) For $n = 2-7$, initial magnetic moment of all atoms have been taken in the same direction, but the final magnetic moment of the structure has been determined after optimization without any constraint. (3) For $n = 2-7$, the system is relaxed using spin-unpolarized GGA. (4) For $n = 2-7$, initial magnetic moment of chain atoms have been assigned as is done in (1), but $\mu = \sum \mu_a$ is not forced to vanish in the course of relaxation. (5) For $n = 2-7$, spin-polarized GGA calculations have been carried out without assigning any initial magnetic moment. (6) We have assigned the magnetic moment ↑↓ ↓↑ for $n = 4$, and ↑↓ ↓ ↓↑ for $n = 5$. Here different spacings between two spin-arrows indicate different bond lengths. This way different exchange couplings

for different bond lengths and hence dimerization is accounted. (7) The initial magnetic moment on atoms ↑↓ ↓↑ ↑↓ for $n = 6$ and ↑↓↑ ↑ ↑↓↑ for $n = 7$ have been assigned. (8) Similar to (7), initial magnetic moment ↑↓↑ ↑↓↑ and ↑↓ ↓↑↓ ↓↑ have been assigned for n=6 and n=7, respectively. Last three initial conditions are taken into consideration due to the fact that different bond lengths of *3d*-TM atoms affect the type of magnetic coupling between consecutive atoms.[25] The initial atomic structures have been optimized for these initial conditions except Cu and Zn. Only first three conditions are consistent with Cu and Zn. As the initial geometry, a segment of n atoms has been extracted from the optimized infinite zigzag chain and placed in a supercell, where the interatomic distance between adjacent chains was greater than 10 Å for all atoms. Our results are summarized in Table 3.3, where the magnetic orders having the same lowest total energy occurred p times from q different initial conditions, are presented. In this respect the magnetic ordering in Table 3.3 may be a potential candidate for the magnetic ground state.

The average cohesive energy of finite-size chains increases with increasing n. In Fig. 3.9, we plot the average cohesive energy of these small segments consisting of n atoms. For the sake of comparison, we presented the plots for the linear and zigzag structures. The average values of cohesive energy in Fig. 3.9(b) are taken from Table 3.3. We note three important conclusions drawn from these plots. (i) The cohesive energy of the zigzag structures are consistently larger than those of the linear structures, and the cohesive energies also increase with increasing n. (ii) For each types of structures, as well as for each n, the variation of E_c with respect to the number of *3d* electrons in the outer shell, N_d, exhibits a double hump shape, which is typical of the bulk and the infinite chain structures as presented in Fig. 3.5. (iii) For specific cases $E_c(n_2) < E_c(n_1)$, even if $n_2 > n_1$ (V and Cr). This situation occurs because the total energy cannot be lowered in the absence of dimerization.

Most of the finite zigzag chain structure of *3d*-TM atoms have a FM lowest energy state. The magnetic ordering specified by AFM* for specific chains indicates that the magnetic moment on individual atoms, μ_a, may be in opposite directions or may have unequal magnitudes, but the total magnetic moment,

Table 3.3: The average cohesive energy E_c (in eV/atom); the net magnetic moment μ, (in Bohr magneton μ_B); magnetic ordering (MO); LUMO-HOMO gap of majority/minority states, $E_G^\uparrow$ and $E_G^\downarrow$, respectively (in eV) for lowest energy zigzag structures. p/q indicates that the same optimized structure occurred p times starting from q different initial conditions.(See text) Results have been obtained by carrying out structure optimization within collinear approximation using the ultra-soft pseudopotentials.

ZZ		Sc	Ti	V	Cr	Mn	Fe	Co	Ni	Cu	Zn
	E_c	0.83	1.38	1.29	0.93	0.32	1.29	1.49	1.38	1.14	0.02
	μ	4.0	2.0	2.0	0.0	10.0	6.0	4.0	2.0	0.0	0.0
$n=2$	$E_G^\uparrow/E_G^\downarrow$	0.59/1.60	0.29/1.01	1.03/1.22	2.17/2.17	2.04/0	1.14/0.59	1.42/0.36	1.48/0.27	1.59/1.59	3.96/3.96
	MO	FM	FM	FM	AFM	FM	FM	FM	FM	NM	NM
	$p\,(q=5)$	2	1	2	1	1	2	2	1	3	3
	E_c	1.30	1.87	1.61	0.91	0.63	1.72	1.84	1.78	1.24	0.12
	μ	1.0	6.0	3.0	6.0	15.0	10.0	7.0	2.0	1.0	0.0
$n=3$	$E_G^\uparrow/E_G^\downarrow$	0.66/0.44	0.45/1.08	0.31/0.78	1.23/2.03	1.66/0.35	0.39/0.58	0.19/0.18	0.87/0.24	0.08/1.55	2.96/2.96
	MO	FM	FM	FM	FM	FM	FM	FM	FM	FM	NM
	$p\,(q=5)$	3	1	2	2	1	2	3	3	1	3
	E_c	1.54	2.13	2.01	1.16	0.84	2.07	2.31	2.08	1.61	0.13
	μ	4.0	2.0	2.0	0.0	18.0	14.0	10.0	4.0	0.0	0.0
$n=4$	$E_G^\uparrow/E_G^\downarrow$	0.37/0.36	0.46/0.50	0.35/0.30	1.16/0.61	1.16/0.50	1.47/0.04	1.98/0.34	1.10/0.25	0.96/0.96	2.35/2.35
	MO	FM	FM	FM	AFM*	FM	FM	FM	FM	NM	NM
	$p\,(q=6)$	5	3	4	4	4	2	1	3	3	3
	E_c	1.63	2.27	2.08	0.83	0.91	2.25	2.46	2.23	1.74	0.15
	μ	3.0	0.0	0.0	0.0	5.0	16.0	11.0	6.0	1.0	0.0
$n=5$	$E_G^\uparrow/E_G^\downarrow$	0.29/0.46	0.43/0.43	0.49/0.40	0.47/0.52	1.12/0.30	1.42/0.56	1.53/0.37	1.47/0.09	1.42/0.90	1.96/1.96
	MO	FM	AFM*	AFM*	AFM*	FM	FM	FM	FM	FM	NM
	$p\,(q=6)$	3	4	2	4	4	1	1	3	1	3
	E_c	1.69	2.32	2.26	1.29	1.02	2.31	2.50	2.29	1.75	0.17
	μ	8.0	0.0	0.0	0.0	0.0	20.0	14.0	6.0	2.0	0.0
$n=6$	$E_G^\uparrow/E_G^\downarrow$	0.22/0.29	0.44/0.44	0.54/0.54	0.53/0.55	0.41/0.38	1.33/0.41	0.30/0.32	0.28/0.10	1.42/0.95	1.88/1.88
	MO	FM	AFM	AFM	AFM*	AFM*	FM	FM	FM	FM	NM
	$p\,(q=7)$	3	3	7	4	4	2	4	4	1	3
	E_c	1.74	2.38	2.22	1.25	1.06	2.35	2.58	2.36	1.84	0.18
	μ	7.0	6.0	5.0	6.0	5.0	22.0	15.0	8.0	1.0	0.0
$n=7$	$E_G^\uparrow/E_G^\downarrow$	0.01/0.33	0.34/0.21	0.32/0.48	0.54/0.68	0.85/0.42	0.95/0.29	0.98/0.17	0.83/0.09	0.79/0.61	1.77/1.77
	MO	FM	FM	FM	FM	FM	FM	FM	FM	FM	NM
	$p\,(q=7)$	5	3	6	4	5	1	2	4	1	3
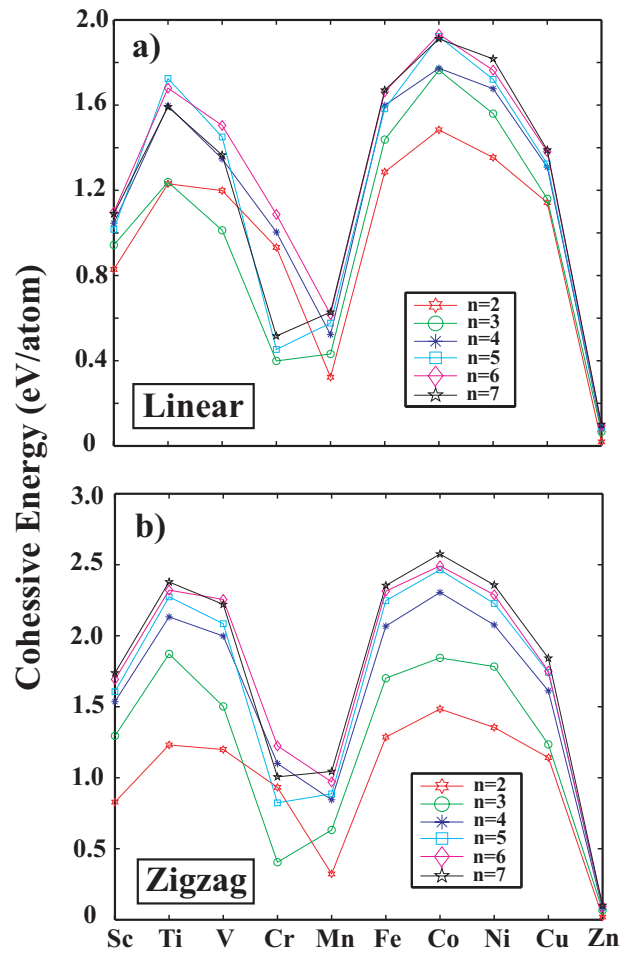
Figure 3.9: Variation of the average cohesive energy of small segments of chains consisting of n atoms. (a) The linear chains; (b) the zigzag chains . In the plot, the lowest energy configurations for each case obtained by optimization from different initial conditions.

$\mu = \sum \mu_a$, adds up to zero. The finite chains of Zn atoms are always nonmagnetic for all n. Finite zigzag chains of Cu are nonmagnetic for even n, except $n = 6$. Interestingly, the dimerized linear chain of Cr ($n = 5$) with a FM lowest energy state is more energetic than that of the zigzag chain given in Table 3.3. The geometry of this structure is such that two dimers consisting of two atoms are formed at both ends of the linear structure and a single atom at the middle is located equidistant from both dimers. The distance from the middle atom to any of the dimers is approximately twice the distance between the atoms in the dimer. Even though the nearest neighbor distance of the middle atom to dimers is long, there is a bonding between them. The cohesive energy is ~ 0.2 eV higher than that of the zigzag case, and the total magnetic moment of the structure (6 μ_B) is provided by the atom at the middle. This is due to the fact that two dimers at both ends are coupled in the AFM order. This is an expected result because the cohesive energy (per atom) of Cr_2 is higher than that of Cr_5 in the zigzag structure. The LUMO/HOMO gap for majority and minority spin states usually decreases with increasing n. However, depending on the type of TM atom, the maximum value of the gap occurs for different number n of atoms. The zigzag chains of Zn atoms usually have the largest gap for a given n.

Even though the total magnetic moment, $\mu = \sum \mu_a$, of the AFM* state vanishes for the finite molecule, LUMO-HOMO gaps for majority and minority states are not generally the same as in the AFM state. This can be explained by examining the magnetic moment on every individual atom and the geometry of the molecule. For Cr_4, the magnetic moment on each atom are lined up as described in the sixth initial condition. In this ordering, two dimers each consisting of two atoms are in the AFM ordering within themselves, but in the FM ordering with each other. The distribution of final magnetic moment on atoms for Mn_6 also obey one of the initial conditions (case 7). Three dimers each consisting of two atoms coupled in the AFM order within themselves, but in the FM order with each other. Similar results are also obtained for other AFM* states.

The zigzag planar structure for $n > 3$ in Table 3.3 corresponds to a local minimum. To see whether the planar zigzag structures are stable, or else it transforms to other geometry by itself is a critical issue. To assure that the finite

chain structures of $n = 4$ and $n = 7$ in Table 3.3 are stable in a local minimum, we first displaced the atoms out of planes, then we optimized the structure. Upon relaxation all displaced atoms returned to their equilibrium position on the plane.

3.3.2 Noncollinear approximation and the spin-orbit interaction

The finite chains discussed in the previous section within collinear approximation will now be treated using noncollinear approximation. To this end, the structure of chains have been optimized starting from the same initial geometry (starting from a segment of n atoms extracted from the optimized infinite ZZ (or ZZD) chain placed in a supercell) and five different initial configurations of spins on individual atoms. (i) The direction of the initial magnetic moment on the atoms are consecutively altered as $xyzy$. (ii) No preset directions are assigned to the individual atoms, they are determined in the course of structure optimization using noncollinear approximation. (iii) For each triangle, the initial magnetic moment on the atoms have a non-zero component only in the xy-plane, but $(\sum_{\triangle} \mu_a)_{xy} = 0$. (Here '$\triangle$' stands for the summation over the atoms forming a triangle) (iv) Similar to (iii), but $(\sum_{\triangle} \mu_a)_z \neq 0$. (v) In a zigzag chain, the magnetic moment of atoms on the down row are directed along z-axis, while those on the up row are directed in the opposite direction. Using these five different initial conditions on the magnetic moment of individual atoms, the initial atomic structure is optimized using both ultra-soft[49] pseudopotentials and PAW[50] potentials. We first discuss the results obtained by using ultra-soft pseudopotentials. Almost all of the total magnetic moment and the cohesive energy of the optimized structures have been in good agreement with those given in Table 3.3 (obtained within collinear approximation). However, there are some slight changes for specific finite structures. For example, Sc_7 is found to have magnetic moment of 7 μ_B in collinear approximation. Even though one of the initial condition in noncollinear calculations resulted in the same magnetic moment and energy, we also found a state which has 0.01 eV lower total energy with the total magnetic moment of 9 μ_B. The same situation also occurred with PAW potential. Ti_5 has a special

Table 3.4: The highest average cohesive energy, E_c (in eV/atom); the components (μ_x, μ_y, μ_z) and the magnitude of the net magnetic moment μ (in μ_B); LUMO-HOMO gap E_G (SO coupling excluded)/ energy gap after spin-orbit coupling was included in $x-$ direction / in $z-$ direction (in eV); magnetic ordering MO; Spin-orbit coupling energy $\triangle E_{so}^x$($/\triangle E_{so}^z$) (in meV) under x and z initial direction of easy axes of magnetization. p ($q = 5$) indicates that the same optimized structure occurred p times starting from q ($= 5$) different initial conditions. Results have been obtained by carrying out structure optimization calculations within noncollinear approximation using PAW potentials. Mn$_7$ is not stable in the planar ZZ structure. For the (x, y, z) directions see Fig. 3.1 (b). These values belong to the most energetic configuration determined by noncollinear calculations including spin-orbit coupling.

ZZ		Sc	Ti	V	Cr	Mn	Co	Ni
$n=2$	E_c	0.85	1.56	1.58	0.53	0.47	1.50	1.60
	(μ_x,μ_y,μ_z), μ	(2.3, 2.3, 2.3), 4.0	(0.0, 0.0, 2.0), 2.0	(1.2, 1.1, 1.2), 2.0	(0.0, 0.0, 0.0), 0.0	(1.1, -0.2, 9.9), 10.0	(2.8, 2.9, 0.0), 4.0	(1.7, 1.0, 0.0), 2.0
	$E_G/E_G^x/E_G^z$	0.49/0.18/0.17	0.36/0.36/0.36	0.67/0.67/0.66	0.56/1.87/1.87	0.18/0.18/0.18	0.05/0.05/0.05	0.18/0.17/0.30
	MO	FM	FM	FM	AFM	FM	FM	FM
	$\triangle E_{so}^x/\triangle E_{so}^z$	3.60/3.80	4.70/3.90	8.30/8.00	10.90/10.90	13.30/13.50	0.01/9.90	33.30/32.50
	$p\,(q=5)$	4	4	5	3	3	5	4
$n=3$	E_c	1.36	2.00	1.91	0.72	0.70	1.90	2.04
	(μ_x,μ_y,μ_z), μ	(0.4, 0.9, -0.1), 1.0	(2.2, 2.3, 2.4), 6.0	(0.6, 0.6, 0.6), 1.0	(5.6, 2.2, 0.0), 6.0	(1.4, -2.7, 0.1), 3.0	(0.3, 0.6, 7.0), 7.0	(0.7, 1.4, 1.3), 2.0
	$E_G/E_G^x/E_G^z$	0.37/0.37/0.37	0.26/0.26/0.25	0.44/0.44/0.44	1.01/1.01/1.01	0.25/0.24/0.24	0.34/0.11/0.12	0.11/0.11/0.10
	MO	FM	FM	FM	FM	FM	FM	FM
	$\triangle E_{so}^x/\triangle E_{so}^z$	3.70/3.70	4.70/4.70	8.40/8.40	10.40/10.50	13.10/13.00	8.20/9.60	33.10/32.70
	$p\,(q=5)$	4	2	3	2	1	1	5
$n=4$	E_c	1.60	2.36	2.35	0.89	1.02	2.29	2.33
	(μ_x,μ_y,μ_z), μ	(0.6, 1.7, 0.9), 2.0	(1.1, 1.2, 1.2), 2.0	(0.0, 0.0, 0.0), 0.0	(0.0, 0.0, 0.0), 0.0	(0.0, 0.0, 0.0), 0.0	(4.6, 4.6, 4.7), 8.0	(-0.8, -2.1, 3.3), 4.0
	$E_G/E_G^x/E_G^z$	0.29/0.29/0.29	0.41/0.41/0.41	0.28/0.28/0.28	1.09/1.09/1.09	0.30/0.30/0.30	0.03/0.03/0.03	0.06/0.21/0.20
	MO	FM	FM	AFM	AFM	AFM	FM	FM
	$\triangle E_{so}^x/\triangle E_{so}^z$	3.70/3.70	4.70/4.70	8.40/8.40	10.30/10.20	13.20/13.20	8.30/8.80	32.10/32.20
	$p\,(q=5)$	3	4	2	1	3	5	2
$n=5$	E_c	1.67	2.49	2.46	1.00	1.22	2.50	2.46
	(μ_x,μ_y,μ_z), μ	(0.8, 0.1, 0.6), 1.0	(0.0, 0.0, 0.0), 0.0	(0.7, 0.5, 0.6), 1.0	(2.5, 2.5, 1.9), 4.0	(-1.3, 1.7, -2.1), 3.0	(-2.4, 10.6, -1.4), 11.0	(2.4, 5.5, -0.1), 6.0
	$E_G/E_G^x/E_G^z$	0.26/0.26/0.26	0.34/0.34/0.34	0.27/0.27/0.27	0.28/0.44/0.44	0.09/0.21/0.21	0.33/0.33/0.33	0.14/0.01/0.01
	MO	FM	AFM	FM	FM	FM	FM	FM
	$\triangle E_{so}^x/\triangle E_{so}^z$	3.80/3.50	4.80/4.80	8.20/8.20	10.40/10.40	14.10/13.00	8.90/8.90	33.90/34.20
	$p\,(q=5)$	4	4	3	1	1	2	5
$n=6$	E_c	1.75	2.53	2.57	1.26	1.31	2.56	2.49
	(μ_x,μ_y,μ_z), μ	(0.0, 0.0, 0.0), 0.0	(0.0, 0.0, 0.0), 0.0	(0.0, 0.0, 0.0), 0.0	(0.0, 0.0, 0.0), 0.0	(0.0, 0.0, 0.0), 0.0	(6.7, 6.7, 7.3), 12.0	(0.0, 0.0, 0.0), 0.0
	$E_G/E_G^x/E_G^z$	0.19/0.19/0.19	0.32/0.32/0.32	0.38/0.38/0.38	0.77/0.77/0.77	0.48/0.48/0.48	0.20/0.20/0.20	0.20/0.17/0.17
	MO	AFM	AFM	AFM	AFM	AFM	FM	AFM
	$\triangle E_{so}^x/\triangle E_{so}^z$	3.70/3.70	4.70/4.70	8.10/8.10	10.30/10.30	13.20/13.30	8.00/8.40	32.30/32.30
	$p\,(q=5)$	1	4	5	4	4	5	5
$n=7$	E_c	1.82	2.60	2.57	1.14		2.65	2.60
	(μ_x,μ_y,μ_z), μ	(5.2, 5.2, 5.2), 9.0	(1.1, 2.8, 0.0), 3.0	(0.1, 1.0, 0.0), 1.0	(-0.2, -0.2, 6.0), 6.0		(8.6, 8.7, 8.7), 15.0	(-2.6, 7.5, 0.3), 8.0
	$E_G/E_G^x/E_G^z$	0.15/0.15/0.15	0.19/0.19/0.20	0.24/0.24/0.24	0.39/0.39/0.39		0.09/0.09/0.09	0.09/0.05/0.05
	MO	FM	FM	FM	FM		FM	FM
	$\triangle E_{so}^x/\triangle E_{so}^z$	3.80/3.80	4.90/4.80	8.20/8.20	10.60/10.40		8.30/8.50	33.70/33.50
	$p\,(q=5)$	2	1	5	2		5	5

magnetic moment distribution which is the same for both ultra-soft and PAW cases and will be explained below. In collinear approximation, V_5 is noted to have zero magnetic moment, nevertheless there is a state 0.03 eV lower in energy which is FM with $\mu = 1$. Even though Co_7 has the same total magnetic moment in both collinear and noncollinear case, there is a significant energy difference between two cases.

Noncollinear calculations have also been performed using PAW potentials (which is necessary for the spin-orbit coupling calculations) starting with five different initial assignment of magnetic moments as described above. Most of our calculations have yielded the same magnetic moment distribution with previous calculations, but there are still few cases, which are resulted differently. Mn_7 is an exception; all structure optimization starting from different initial conditions resulted in a non-planar geometry. Note that in collinear and noncollinear calculations using ultra-soft pseudopotential Mn_7 was stable in a local minimum corresponding to the planar zigzag geometry, but it formed a cluster when spin-orbit coupling and noncollinear effects are taken into account by using PAW potentials. Unlike other $n = 5$ zigzag structures, Ti_5 has a unique ordering of the atomic magnetic moments. Two Ti atoms on the upper row have magnetic moments which are in opposite direction. Similarly, two Ti atoms at the ends of the lower row also have atomic magnetic moments in opposite direction, but the magnitude of moments are smaller than those of on the upper row. The atom at the middle of the lower row has no magnetic moment. In $n = 6$ case, only Co_6 has a non-vanishing magnetic moment. Other atoms form dimers which are coupled in the AFM order. If we assume that the shape of $n = 6$ molecule is parallelogram, there is an AFM coupling between the atoms on both diagonals. In addition to these, remaining two atoms in the middle also coupled in the AFM order as indicated in Fig. 3.10. Cr_n chains exhibit an even-odd disparity; Cr_n has an AFM ordering for even n, but it has a FM ordering for odd n. There are also cases where collinear and noncollinear calculations with ultra-soft pseudopotential resulted in an excited state for the magnetic moment distribution. Although PAW potential calculations found the same magnetic ordering with collinear and ultra-soft noncollinear cases, there are even more energetic states for Sc_6, V_4, Cr_5
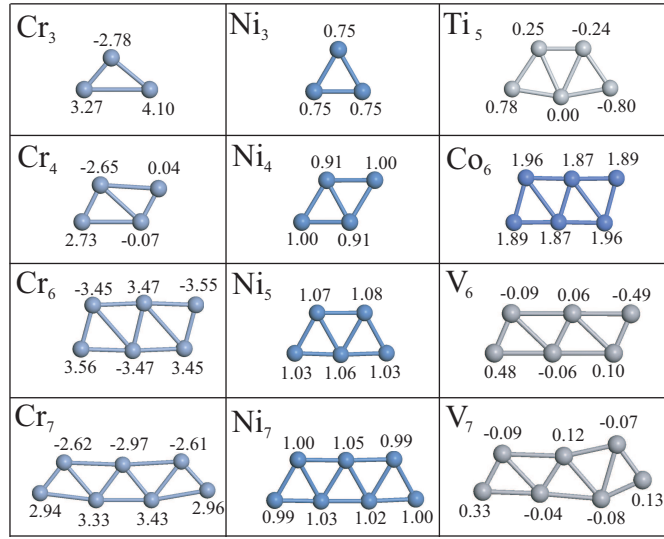
Figure 3.10: The atomic magnetic moments of some finite chains of *3d* transition metal atoms. Numerals on the atomic sites stand for the value of the atomic magnetic moments. Positive and negative numerals are for spin-up and spin-down polarization, respectively. Because of finite-size of the zigzag chains, the end effects are usually appear by different values of magnetic moments on atoms at the end of the chain.

and Mn_5 given in Table 3.4. Geometric dimerization also plays an important role in determining the average cohesive energy. Due to the magnetic ordering and the dimerization of atoms in the finite molecules, the average cohesive energy may not always increase as the number of atoms in the molecule increases. V_6 and V_7; Cr_6 and Cr_7; Ni_5 and Ni_6 are examples where magnetization and dimerization effects are most pronounced. It should be denoted that Hobbs *et. al*[41] carried out noncollinear calculations with the PAW potential on Cr_{2-5} and Fe_{2-5} finite chain structures. Here, our results on Cr_{2-5} are in agreement with those of Hobbs *et. al.*[41]

Among several *3d*-atomic chains, Ni_6 and Mn_6 are only chains for which non-collinear effects are most pronounced. For the other structures, noncollinear magnetic moments on the atoms deviate slightly from the collinear case.

We calculated the effects of spin-orbit (SO) coupling energy, as well. In making fully self-consistent calculations, we first assumed that initial easy axis of
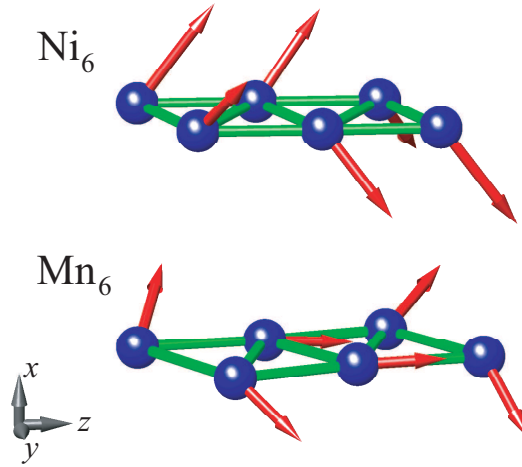
Figure 3.11: Atomic magnetic moments of Ni_6 and Mn_6 planar zigzag chains calculated by noncollinear approximation including spin-orbit interaction. The magnitudes and directions of magnetic moments are described by the length and direction of arrows at each atom.

magnetization of the structure is along $x-$ or $z-$ direction. As shown in Fig. 3.1 (b), $x-$ direction is perpendicular to the plane of atoms and $z-$ direction is the axis along the chain. This way, spinor wave functions are let rotate from their initial orientation until the magnetic moment is parallel to the easy axis of magnetization which is determined in the course of structure optimization. Here, the optimized structure of every initial condition together with the calculated magnetic moment on the individual atoms are used for the calculation of SO coupling. The optimized structures of $(TM)_n$ and atomic magnetic moments have been determined within noncollinear approximation using PAW potentials. Spin-orbit coupling energy is defined by the expansion, $\triangle E_{so}^{x/z} = (E_T^{x/z} - E_T^o)/n$, where $E_T^{x/z}$ and E_T^0 are the total energies of the chain calculated within noncollinear approximation with and without spin-orbit interaction in the $x - /z-$ direction, respectively. The highest average cohesive energy E_c given in Table 3.4 is obtained using the expression $E_c = (nE_a - E_T^{x/z})/n$, where E_a is the ground state energy of the free constituent TM atom. $E_T^{x/z}$ is the lowest value of E_T^x and E_T^z. As it can be easily seen that SO coupling does not play an important role on the energy of the planar finite structure. However, SO coupling becomes crucial

when the total magnetic moments, which happen to be oriented in different directions owing to the different initial conditions, result in the same energy. It is easily observed that in most of the structures both initial direction of easy axis of magnetization resulted in the same SO coupling energy. This means that it is the most probable that fully self-consisted structure optimization of SO coupling calculations resulted in the lowest energy easy axis of magnetization. For this reason other initial directions of easy axis of magnetization was not calculated. In addition $\triangle E_{so}^x$ and $\triangle E_{so}^z$ appear to be independent of n except Mn_5, Co_2 and Co_3. It is also observed that when SO coupling is taken into account, LUMO-HOMO gap energies decrease. Only for Ni_4, Cr_5, Mn_5 and Ni_7, LUMO-HOMO gap increased due to the fact that the final geometry of SO coupling calculations has further relaxed slightly from that of noncollinear calculations.

Chapter 4

Electronic and Magnetic Properties of Cr Nanowires

Scientist are working on determining the physics of nanoscale metal nanowires. Experimentally obtaining nanowire structures are quite advanced and many structures already have been synthesized, but theoretical investigations are far behind the experimental findings. The electronic and magnetic properties of one dimensional nanowire structures in experiments display various and different character from bulk structures and expected to be a promising transport material in junctions of many different electronic nanodevices. Not only the transport phenomena, but also the most of the conventional electronics nowadays is based on the transport of information through charges and new generation devices are expected to take the advantage of the electron spin to double the capacity of electronics. The TM atomic chains discussed in the present thesis are only precursors; any application requires having a cross section thicker than a single atom.

As a further step towards more realistic systems we investigated structural, electronic and magnetic properties of Cr nanowires using first-principles pseudopotential plane wave calculations. All Cr-nanowires studied are metals and have ferrimagnetic ground state. The type of coupling, as for ferromagnetic or antiferromagnetic, between neighboring Cr atoms depends on their distance. We

also examined noncollinear magnetism together with spin-orbit interaction and concluded that easy axis of magnetization plays an important to determine the ground state magnetic structure.

4.1 Method of calculations

We have performed first-principles plane wave calculations[38, 47] within Density-Functional Theory (DFT)[48] using PAW[50] potentials both for the collinear and noncollinear spin-orbit calculations of nanowire structures. The exchange-correlation potential has been approximated by generalized gradient approximation (GGA).[51] For the partial occupancies, we have used the Methfessel-Paxton smearing method.[52] The width of smearing for the infinite structures has been chosen as 0.01 eV for geometry relaxations and the accurate energy band and the density of state (DOS) calculations. We treated the nanowire structures by supercell geometry (with lattice parameters a_{sc}, b_{sc}, and c_{sc}) using the periodic boundary conditions. A large spacing (~ 10 Å) between the adjacent nanowires has been assured to prevent interactions between them. Calculations are carried on both single and double cell nanowire structures. In all calculations of Cr nanowires (CrNW), c_{sc} has been taken to be equal to the lattice constant of the chain. The number of plane waves used in expanding Bloch functions and **k**-points used in sampling the Brillouin zone (BZ) have been determined by a series of convergence tests. Accordingly, in the self-consistent potential and the total energy calculations the BZ has been sampled by (1x1x27) mesh points for single cell calculations in **k**-space within Monkhorst-Pack scheme. [40] For double cell calculations (1x1x13) mesh points are taken in **k**-space. A plane-wave basis set with the kinetic energy cutoff $\hbar^2|\mathbf{k} + \mathbf{G}|^2/2m = 350$ eV has been used. The convergence of the system is achieved when the difference of the total energies of last two consecutive steps is less than 10^{-5} eV and the maximum force allowed on each atom is 0.03 eV/Å. The total energy of the optimized structure (E_T) relative to free atom energies is negative, if it is in a binding state. As a rule, the structure becomes more energetic (or stable) as its total energy is lowered. Figure 4.1 describes various chain structures of TM atoms treated in this study.

In calculations involving PAW potentials, kinetic energy cutoff is taken as 400 eV. All the atomic positions and lattice constants (c_{sc}) have been optimized by using the conjugate gradient method where the total energy and the atomic forces are minimized. The convergence is achieved when the difference of the total energies of last two consecutive steps is less than 10^{-5} eV and the maximum force allowed on each atom is 0.05 eV/Å. As for the finite structures, supercell has been constructed in order to assure $\sim$ 10 Ådistance between the atoms of adjacent finite chain in all directions and BZ is sampled only at the Γ-point. The other parameters of the calculations have been kept the same. The total energy of the optimized structure (E_T) relative to free atom energies is negative, if it is in a binding state. As a rule, the structure becomes more energetic (or stable) as its total energy is lowered. Figure 4.1 describes two different nanowire structures and infinite periodic planar chains.

We have performed finite-temperature ab initio molecular dynamics calculations up to 900 K using the Nosé[57] thermostat for 300 time steps (3 fs each time step) to check whether the optimized structure will be affected from random thermal motion of atoms or whether they maintain their tubular form at high temperatures. We believe that if there were any kind of structural instability, it would be initiated and also enhanced within these time steps at high temperatures.

4.2   Cr Infinite Monatomic Chain Structures

In the previous section, we have investigated the magnetic and electronic properties of all *3d* TM monatomic chains and finite size (number of atoms ranges from 2 to 7) molecules. From all of these observations, we can conclude that chromium has properties which are different from other observed TM. In this part, we give a brief summary of the magnetic and electronic properties of Cr monatomic chains for the sake of comparison and to emphasis why Cr nanowires might be good candidate for future magnetic devices.
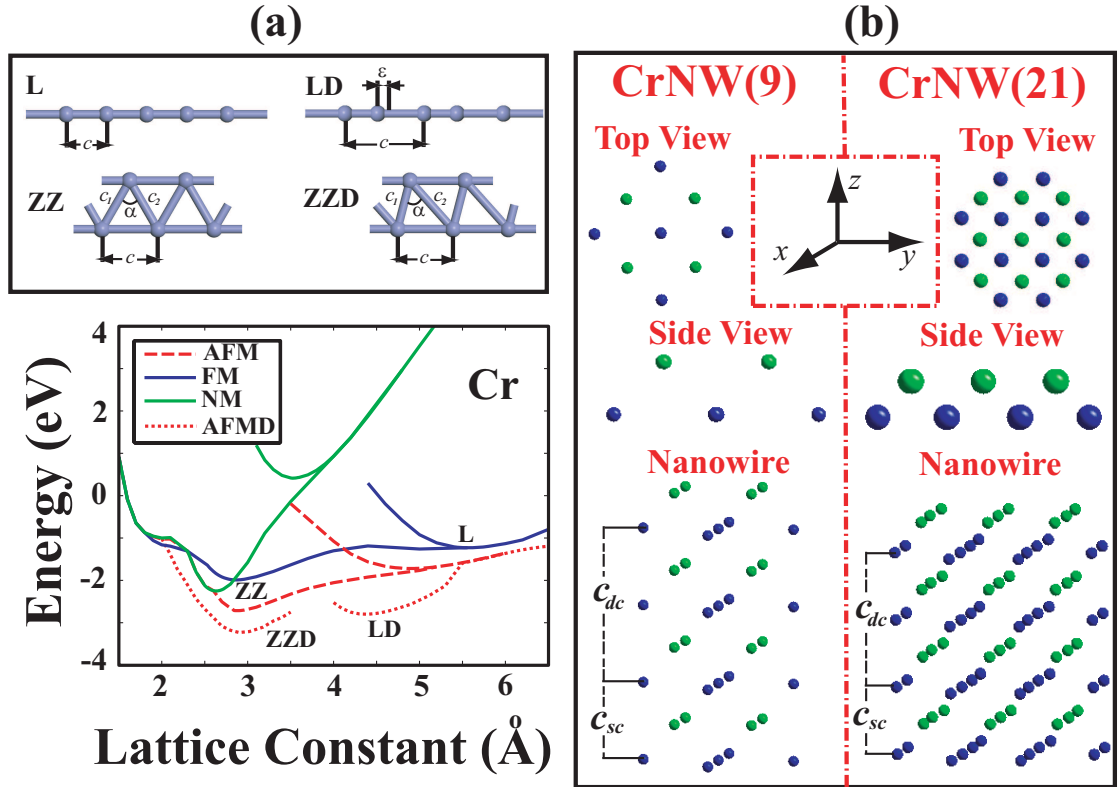
Figure 4.1: Various structures of Cr monatomic chains. (a) Infinite and periodic structures; L: The infinite linear monatomic chain of Cr with lattice constant, c. LD: The dimerized linear monatomic chain with two Cr atoms in the cell. ϵ is the displacement of the second atom from the middle of the unit cell. ZZ: The planar zigzag monatomic chain with lattice parameter c and unit cell having two Cr atoms. $c_1 \sim c_2$ and $59^0 < \alpha < 62^0$. ZZD: The dimerized zigzag structure $c_1 \neq c_2$. (b) Structures of Cr nanowires consisting of 9 and 21 atoms in a unit cell.

Figure 4.1 (a) shows the energy versus lattice constant of Cr infinite and periodic chain structures in different magnetic states. These are the infinite linear (L), the dimerized linear (LD), the planar zigzag (ZZ), and the dimerized zigzag (ZZD) monatomic chains which are also indicated in the upper part of Fig. 4.1. In calculation of the ferromagnetic (FM) state, the structure is optimized each time using a spin-polarized GGA calculations starting with a different preset magnetic moment in agreement with Hund's rule. The relaxed magnetic moment yielding to the lowest total energy has been taken as the FM state of the chain. For the antiferromagnetic (AFM) state, we assigned different initial spins of opposite directions to adjacent atoms and relaxed the structure. We performed spin-unpolarized GGA calculations for the nonmagnetic (NM) state. The binding energy per Cr atom relative to the free constituent atoms is expressed as $E_b = [NE_a - E_T]/N$, in terms of the total energy per unit cell of the given chain structure for a given magnetic state (E_T) and the ground state energy of the free constituent TM atom, E_a. From this representation $E_b < 0$ for Cr atom corresponds to a binding structure, but not necessary to a stable structure. The cohesive energy per atom is $E_c = -E_b$.

Not only Cr has LD and more energetic ZZD structures in the AFM state, but also the displacement of the second atom from the middle of the unit cell, ϵ, is rather large for the dimerized linear chain structure of Cr. In addition to these Cr is the only element which has AFM lowest energy state for both linear and zigzag structures. Apparently, the dimerization is stronger than the usual Peierls distortion. As a result, the nearest neighbor distance, $(c-\epsilon)$, is much smaller than the second nearest neighbor distance, $(c+\epsilon)$. This situation poses the question whether the interaction between the adjacent dimers are strong enough to maintain the coherence of the chain structure. We address this question by comparing the energies of individual dimers with the chain structure. The formation of the LD structure is energetically more favorable with respect to individual dimer by 0.54 eV per atom. Furthermore, the charge accumulation, namely the positive part of the difference between the charge density of the interacting system and that of the non-interacting system, presented in Fig. 4.2 (b), indicates a significant bonding between the adjacent dimers. On the other hand the bonding in a

Table 4.1: The average cohesive energy E_c (in eV/atom); lattice constant c (in Å); displacement of the middle atom in LD structure ϵ (in Å), ratio of the first nearest neighbor, c_1 (in Å) and the second nearest neighbor c_2 (in Å) for ZZD structure [(c_1/c_2) unitless]; magnetic ground state MGS; and the total magnetic moment, μ per unit cell (in Bohr magnetons, μ_B) obtained within collinear approximation.

	Cr LD	Cr ZZD
E_c	1.40	1.57
c	4.40	2.90
$\epsilon/\ (c_1/c_2)$	0.66	0.59
MGS	AFM	AFM
μ	±1.95	±1.82

dimer is much stronger than the one in a L chain. Nevertheless, the LD structure has to transform to more energetic ZZD structure. The zigzag structures in the AFM, FM and NM states have minima at higher binding energies and hence are unstable.The cohesive energy, lattice constant, total magnetic moments, magnetic ground states can be found in Table 4.1.

Figure 4.2 (a) presents the energy band structure of L, LD, ZZ and ZZD geometries. It can be easily concluded that chromium L and LD structures are AFM semiconductors where as all zigzag structures are AFM metals. Finite size molecules of Cr also have interesting behaviors. For example Cr_4, which has a vanishing total magnetic moment for AFM* state indicated in the previous chapter, has LUMO-HOMO gaps for majority and minority states which are not generally the same as in the AFM state.This can be explained by examining the magnetic moment on every individual atom and the geometry of the molecule. The distribution of the magnetic moment on each atom of Cr_4 is found as follows: Two dimers each consisting of two atoms are in the AFM ordering within themselves, but in the FM ordering with each other. Cr_n chains exhibit an even-odd disparity; Cr_n has an AFM ordering for even n, but it has a FM ordering for odd n. Geometric dimerization also plays an important role in determining the average cohesive energy. Due to the magnetic ordering and the dimerization of atoms in the finite Cr molecule, the average cohesive energy may not always increase as the number of atoms in the molecule increases. Cr_6 and Cr_7 is an example
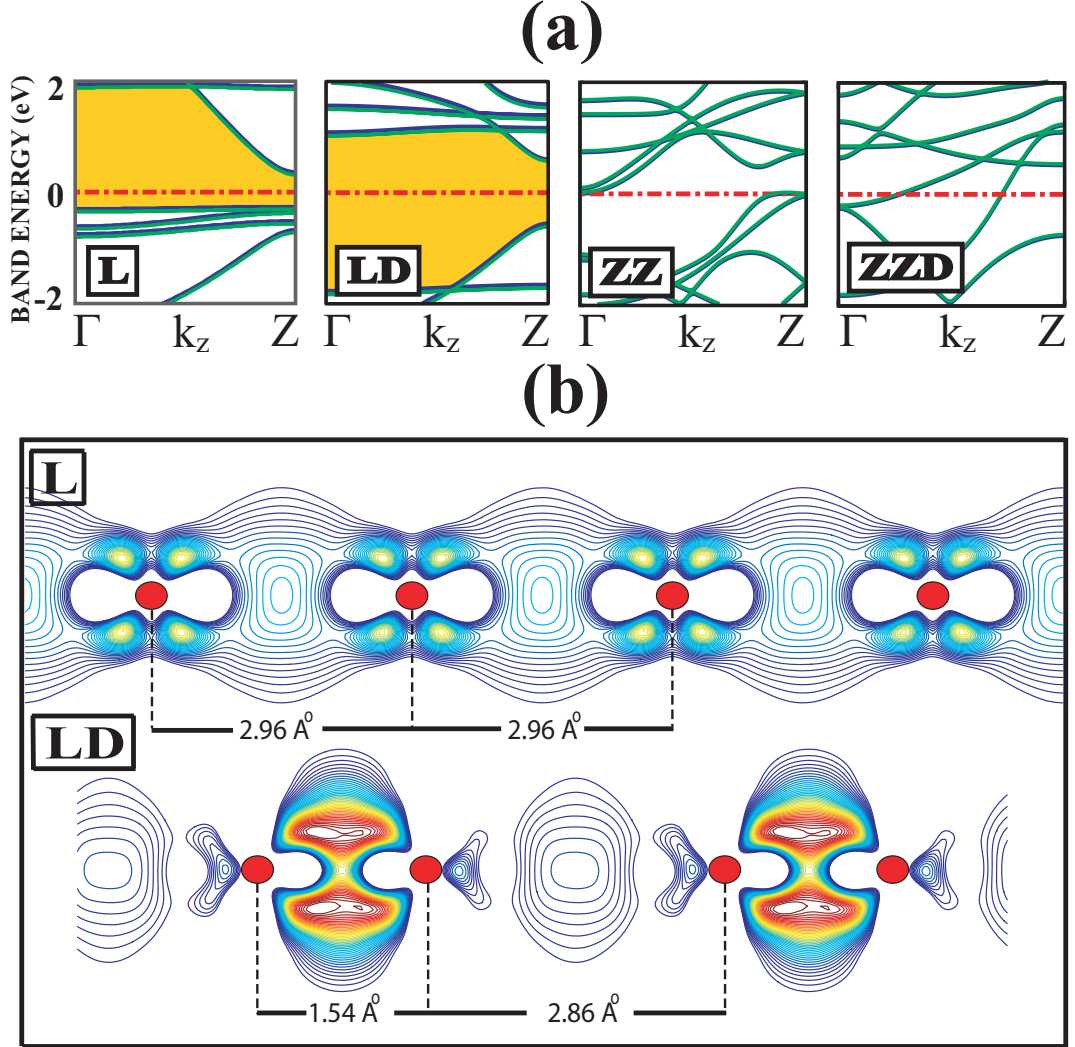
Figure 4.2: (a) Energy band structures of Cr monatomic chains in its L, LD, ZZ and ZZD structures. The zero of energy is set at the Fermi level. Gray and black lines are minority and majority spin bands, respectively. The gray and dark lines coincide in the antiferromagnetic state. The energy gap between the valence and the conduction bands is shaded.(b) The plot of charge accumulation, namely the positive part of the difference between the charge density of the interacting system and that of the non-interacting system, for the linear (L) and the dimerized linear structure (LD) of Cr monatomic chains. Contour spacings are equal to $\Delta\rho = 0.0827e/\text{Å}^3$. The outermost contour corresponds to $\Delta\rho = 0.0827e/\text{Å}^3$. Dark balls indicate Cr atom.

where magnetization and dimerization effects are most pronounced. As a result, it can be concluded that magnetic and electronic properties of Cr monatomic chains and finite size molecules differs significantly from other *3d* TM molecule and chain structures.

4.3   Various size Chromium Nanowires

In this part we will discuss structural having cross section larger than that of Cr atomic chains, elastic, electronic and magnetic properties of 2 different chromium nanowires. Chromium has bcc [55] lattice for bulk structure. Nanowires are obtained from cutting the bulk structure in [001] direction with varying thicknesses and atoms on the edges are removed. The first Cr nanowire (CrNW) we considered contains 9 atoms in a unit cell [CrNW(9)] and the second kind has 21 atoms [CrNW(21)] in a unit cell. The structures are indicated in Fig. 4.1 (b). In both structures, unit cell consists of 2 layers of Cr atoms. In Fig 4.1 (b), gray Cr atoms represents the atoms on the upper layer and black atoms states for the atoms on the lower layer. CrNW(9) has 4 atoms in the upper layer, whereas CrNW(21) contains 9 atoms in the upper layer. We have placed a vacuum (10 Å) between the neighboring CrNWs to minimize the interaction between them. Geometry optimizations are taken place on varying the lattice constant in $z-$ direction in which all atoms in the CrNW are relaxed in every direction. For single cell calculations lattice constant c_{sc} is relaxed, where as in double cell calculations c_{dc} is used where $c_{dc} = 2c_{dc}$. See Fig. 4.1 (b).

4.3.1   Structure Optimization

We have carried out structure optimization calculations for various magnetic states of the nanowire. In calculation of nonmagnetic (NM) state, we performed spin-unpolarized GGA calculations. For ferromagnetic (FM) case, the structure is optimized each time using a spin-polarized GGA calculations starting with a present magnetic moment in agreement with Hund rule. In antiferromagnetic

(AFM) case, neighboring atoms in the unit cell are coupled antiferromagnetically between each other. The amplitude of the initial magnetic moment has been taken according to the Hund rule. In all of the magnetic calculations, the final structure, energy and magnetic moments are calculated in the course of structure optimization without any restriction on magnetic moment and the energy. Noncollinear magnetic and spin-orbit coupling calculations are also included in this study. Systems which have magnetic ground state in collinear approximation, the structure is further optimized by NC calculations. Charge distributions obtained in collinear magnetic states are modified by noncollinear formalism. The initial easy axis of magnetization is assumed to lie in [001] directions, but spinor wave functions are let rotate from their initial orientation until the magnetic moment is parallel to the easy axis of magnetization which is determined in the course of structure optimization.

In Fig. 4.3, we have given variation of binding energy of single and double cell lattice structures with respect to the lattice constant c_{sc} and c_{dc} for CrNW(9). Change of magnetic moment with c_{sc} is also indicated. For both single and double cell structures, lowest energy state is calculated to be FM. In single cell calculations, initially AFM coupled state prefers NM magnetic moment distribution, whereas in double cell calculations, this state makes a transition from FM coupling to NM coupling. The binding energy per atom for both single and double cell calculations resulted in very similar energies which are calculated to be 2.68 eV. In single cell calculations, FM state is favorable from AFM and NM states by 50 meV which is not very high when compared with the room temperature conditions. Lattice constants are also in agreement within each other. Lattice constant, c_{dc}, for double cell structure is just twice of the lattice constant, c_{sc}, obtained in single cell calculations. Considering the magnetic moments of the lowest energy state configurations, one can conclude that doubling the unit cell structure increases the magnetic moment of the structure more than twice. Total magnetic moment on single cell is calculated as $2.96\mu_B$, but this value increases to $6.17\mu_B$ in double cell calculations. This can be due to the fact that in single cell calculations there are only two layers of atoms in the unit cell that have magnetic coupling, but in double cell calculations this value increases to 4. This way,
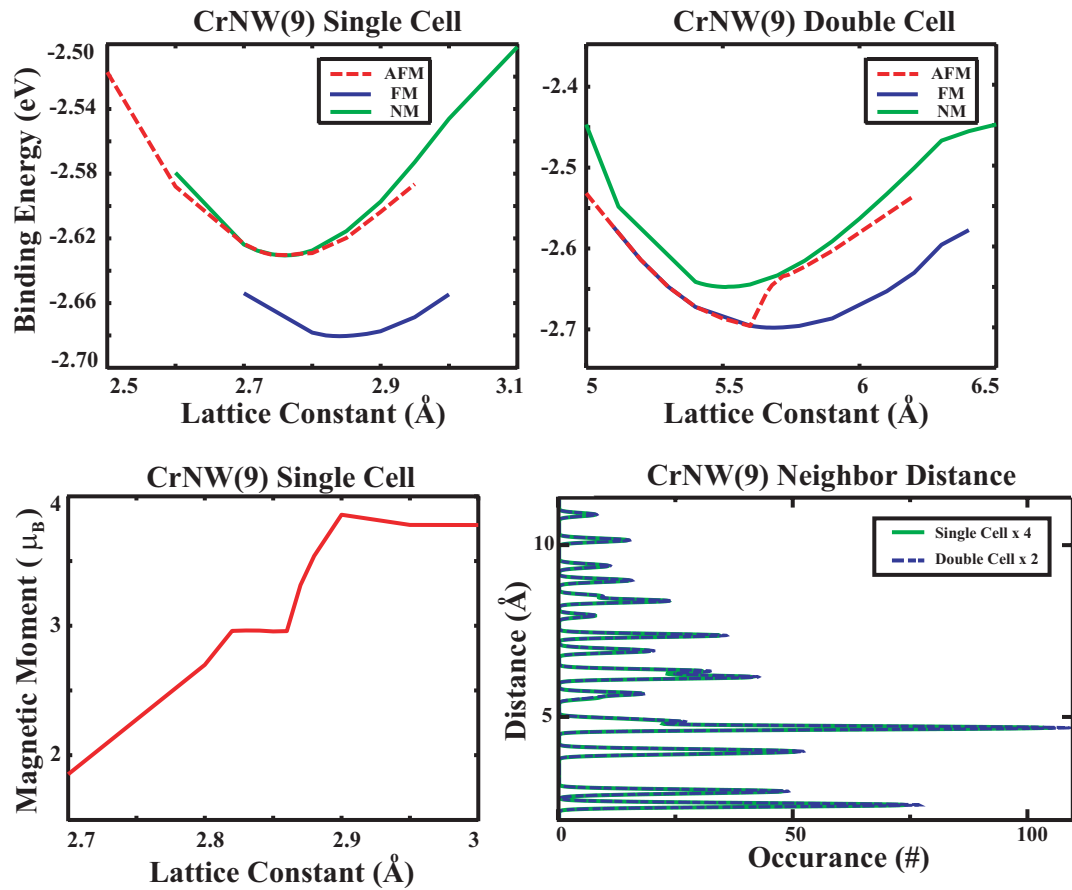
Figure 4.3: (Upper panels) Variation of binding energy with respect to the lattice constant for single and double cell CrNW(9) structures. Change of total magnetic moment for single cell CrNW(9) is also indicated. Distribution of interatomic distance both for single and double CrNW(9) structures are shown. (lower panel)

we also included the magnetic coupling of atoms in distant layers in a unit cell. Exchange-correlation energies are also reduced slightly going from single cell to double cell structures. Triple and quadruple cell calculation may yield better results, but they are computationally expensive and excluded in this study. Radius of CrNW structures are calculated as the maximum distance between the atoms in the same layer. We have also achieved very similar results for both single and double cell calculations. Radii are calculated as 5.59 $\mathring{A}$ and 5.56 $\mathring{A}$ respectively. All of these comparisons between single and double cell structures are done to understand if there is reconstruction on the surface of CrNW. We finalize this by plotting the interatomic distance of CrNW(9) of both single and double cells in Fig. 4.3. This plot is achieved by calculating the interatomic distance of atoms in 4 single cell and 2 double cell structures. The figure indicates that neighbor distances are very similar to each other. In conclusion, there is no reconstruction on the surface of CrNW(9).

Variation of total magnetic moment with c_{sc} also reveals interesting properties of CrNWs. Upon in elongation or compression (c_{sc} is larger or smaller than the lowest energy state), the magnetic moment differs greatly. It can be concluded that as the lattice constant c_{sc} increases, the total magnetic moment of the system generally increases. By this way, CrNW(9) can be use as a detector for determining elongation and compression in the structure. Spring constants of single and double cell CrNW(9)s are also calculated, after making a quadratic fitting to the total energy-lattice constant plot and calculating the second derivative of the plot. The estimated value for single cell CrNW(9) is 21.45 $eV/\mathring{A}^2$, whereas this value reduces to 10.20 $eV/\mathring{A}^2$. It can be deduced that Hooke's Law is still valid in this nanoscale structure. The cohesive energy, lattice constant, spring constant, total magnaetic moments, radius of CrNW(9) and CrNW(21) for both single and double cell structures can be found in Table 4.2.

Structural properties of CrNW(21) is also indicated in Fig. 4.4. For both single and double cell structures, AFM and FM magnetic structures resulted in the same binding energy and final total magnetic moment. The magnetic moment distribution on the atoms of CrNW(21) is neither ferromagnetic nor antiferromagnetic. They are distributed in ferrimagnetic order which will be explained in
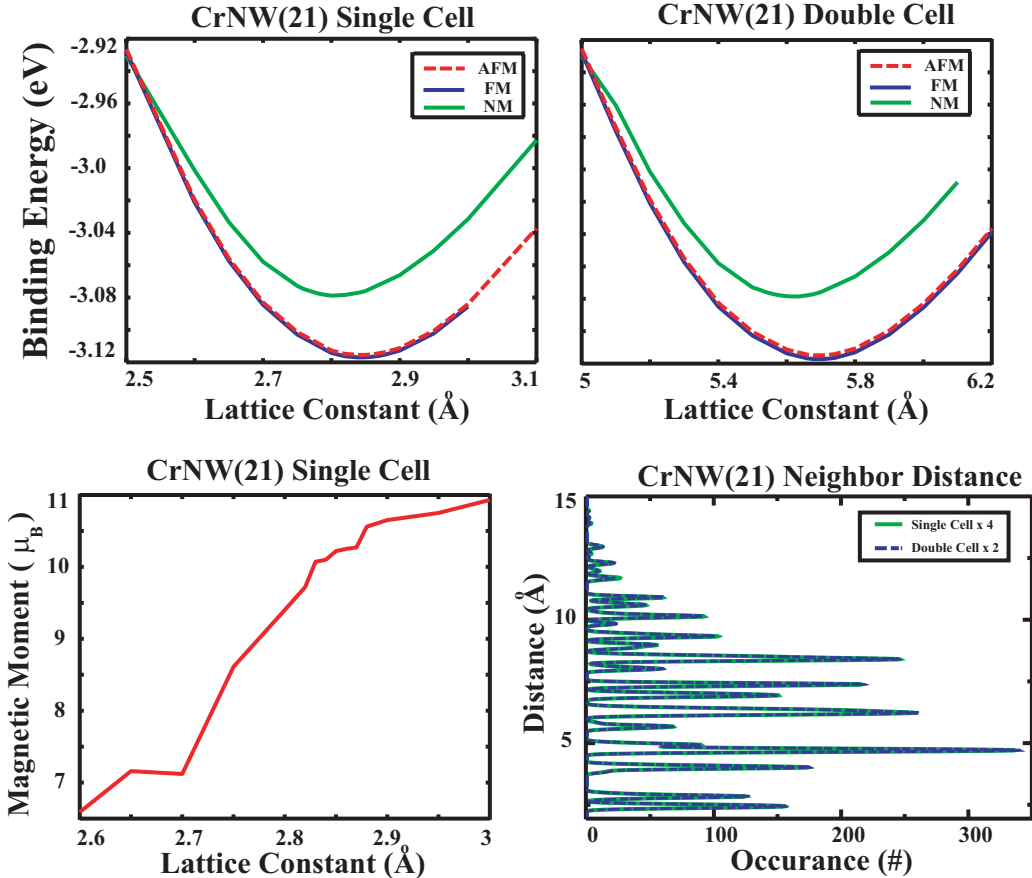
Figure 4.4: Variation of binding energy with respect to the lattice constant for single and double cell CrNW(21) structures. (upper row) Change of total magnetic moment for single cell CrNW(21) is also indicated. Distribution of interatomic distance both for single and double CrNW(21) structures are shown. (lower row)

Table 4.2: The average cohesive energy E_c (in eV/atom); lattice constant for single cell structure c_{sc} (in Å) and for double cell structure c_{dc} (in Å); the total magnetic moment, μ per unit cell (in Bohr magnetons, μ_B); spring constant k (in $eV/\mathring{A}^2$) and the radius of the nanowire structures r (in Å)

	CrNW(9)		CrNW(21)	
	Single Cell	Double Cell	Single Cell	Double Cell
E_c	2.68	2.68	3.11	3.11
c_{sc}/c_{dc}	2.84	5.68	2.84	5.69
μ	2.96	6.17	10.10	20.91
k_{sc}/k_{dc}	21.45	10.20	62.12	30.54
r	5.59	5.56	8.90	8.89

detail in 'Electronic and Magnetic Properties' section. The cohesive energies for both single and double cell structures are calculated as 3.11 eV which is 0.43 eV larger than that of CrNW(9). As the thickness of the structure increases from linear to CrNW(21), the cohesive energy increases significantly due to decreasing surface/volume ratio. It can also be concluded that the stability of the system increases as the number of atoms in the unit cell increases. The energy difference between NM and magnetic states for CrNW(21) is 38 meV, which is even smaller than that of CrNW(9). Total magnetic moment of the system increased extensively as the CrNW gets thicker due to increased in the number of atoms in the unit cell. Similar observations are also carried out in CrNW(21) structure. Doubling the unit cell of CrNW(21) not only increased the total magnetic moment more than twice, but also there is a slight change in the lattice constants of unit cell. From the plot of the comparison of the interatomic distances between 4 single cell and 2 double cell structures and cohesive energy vs lattice constant plots, one can conclude that there is no reconstruction (involving double cell) on the surface of CrNW(21).

Variation of total magnetic moment for CrNW(21) with c_{sc} also reveals that by monitoring the magnetic moment of the system, one can determine if the system is in elongation and compression situation. There is almost a linear relation between the lattice constant c_{sc} and the total magnetic moment. As the lattice constant increases, total magnetic moment of the system increases. To conclude

this subsection, we can say that all the CrNW examined in this study have ferrimagnetic ground states. By doubling the unit cell and making various test, we found that there in no reconstruction on the surface of CrNWs. One can also use CrNW as to measure the elongation and compression of a system by monitoring the total magnetic moment of the CrNW.

4.3.2 Stability and Elastic Properties

Cohesive energy is usually referred to decide the stability of a system. As cohesive energy increases, the system under observation can be assumed to be more stable. The cohesive energy per atom of bcc lattice structure Cr atom is 4.10 eV.[55] CrNW(9) and CrNW(21) have cohesive energies as 2.68 eV and 3.11 eV, respectively. However, whether these geometries correspond to global minima, or local minimum is separated by a significant barrier and requires further investigation. In this thesis, we have checked the stability of CrNW(9) which is less stable than CrNW(21) when cohesive energies of systems are compared. We have followed two different methods to test the stability of CrNW(9). First case is Molecular Dynamics (MD) calculations and other one is varying the distance between two consecutive unit cells of CrNW(9).

Periodic structures of the same kind are always more stable than finite molecule structures because the number of surface atoms in a molecule which have dangling bonds are always greater than its periodic structure. For example, periodic CrNW(9) is more stable than a CrNW(9) molecule which is obtained from placing a vacuum ($\sim 10\mathring{A}$) between two consecutive CrNW(9) unit cells. In this study, we have tested the stability of 2 molecules. First one is obtained by placing a vacuum ($\sim 10\mathring{A}$) in every 3 unit cells. This molecule contains 27 Cr atoms [CrM(27)] and it is not symmetric in $z-$ direction because CrNW(9) contains 2 layers of atoms where layers contains 4 and 5 atoms. To make the molecule symmetric we have placed a layer of Cr atoms that contains 5 atoms for the second molecule. This second molecule contains 32 Cr atoms [CrM(32)]. We have performed finite-temperature ab initio molecular dynamics calculations for both molecules, CrM(27) and CrM(32) using the Nosé[57] thermostat for 300

time steps to check whether the optimized structure will be affected from random thermal motion of atoms or whether they maintain their tubular form at high temperatures. For each structure, we have carried out 3 different MD calculations at various temperature ranges. At first in 300 time steps, we have increased the temperature of the molecule from 0 K to 900 K. In the second MD calculation, the temperature of the molecule is kept at 900 K for 300 time steps and in the last MD calculation, the temperature is reduced to 0 K from 900 K. The length of time step is intentionally taken as 3 fs which is long for a MD calculation, but if the system is unstable, long time steps can break down the geometry of the structure easier. From all of MD calculations those were done to CrM(27) and CrM(32), the geometry of the structures did not affect from the change of the temperature. The distance between Cr atoms decreased because the molecule is cut from periodic CrNW(9). We believe that if there were any kind of structural instability, it would be initiated and also enhanced within these time steps at high temperatures.

Other method we followed is changing the interlayer distance between two consecutive unit cells of CrNW(9) as indicated in Fig. 4.5. Dimerization plays an important role infinite and finite monatomic chain structures. In some cases, the dimerization of Cr atoms are so strong that it may even cause us to question the bonding of some Cr atoms. In previous subsections, we have stated that even though dimerization is effective in Cr monatomic chains, there is a weaker bonding between the dimers. While optimizing the structure, we were expecting to achieve some dimerized Cr atoms in the relaxed structure of CrNW(9) and CrNW(21) which can rather increase the cohesive energy of a Cr atom. Neither relaxed geometries of CrNW(9) nor CrNW(21) have dimerized Cr atoms. To compare the cohesive energies of dimerized and periodic CrNW(9), we placed a varying size vacuum between consecutive CrNW(9) unit cells. The binding energy per atom and the total magnetic moment of the structure is indicated in 4.5 (a). As the dimension of the vacuum between 2 unit cells increases, the cohesive energy of a Cr atom decreases linearly up to $d = 2.5 \mathring{A}$. After $d = 5 \mathring{A}$, the binding energy of a Cr atom does not change. There is also a variation in the total magnetic moment. It first increases and then decreases and acts like hump. After

(a)

CrNW(9) Elastic Properties

(b)
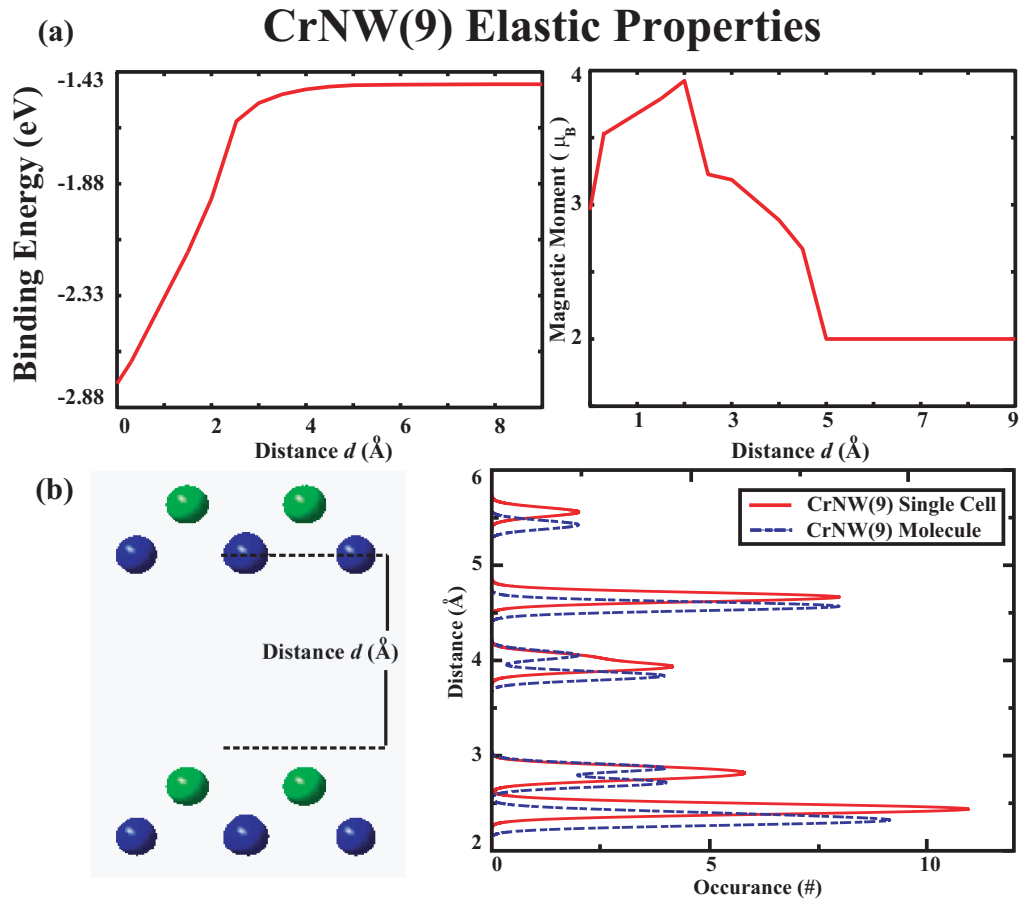
Figure 4.5: (a)Variation of total energy and total magnetic moment as the distance between two consecutive unit cell increases. (b) A sketch of the new structure with varying distance d. Plot of interatomic distances for CrNW(9) and CrNW(9) molecule.

$d = 5\mathring{A}$, it stays unchanged. It can be concluded that after $d = 5\mathring{A}$, there is no interaction between two consecutive unit cells. Cr atoms in a unit cell begins to act like a small molecule. In every different d values, we monitored the geometry of the CrNW(9). We deduce that as d increases, geometric dimerization began to appear and influenced the electronic and magnetic properties of CrNW(9). The dimerization appears as follows: Edge atoms in the first layer of CrNW(9) (having 5 Cr atoms) dimerizes with the closest Cr atom on the other layer (having 4 Cr atoms). The interatomic distances indicated in Fig. 4.5 where d is taken as $9\mathring{A}$(b) shows that the interatomic distances gets smaller due to geometric dimerization. The cohesive energy of periodic CrNW(9) ($d = 0\mathring{A}$) is energetically 1.19 eV favorable than Cr molecule consisting of 9 atoms. The magnetic moment distribution in Cr molecule is rather different. The dimerized Cr atoms coupled antiferromagnetically between each other. The total magnetic moment of the Cr molecule is supplied from the atom that is left in the middle of the layer consisting of 5 atoms. In conclusion, dimerized structures of CrNW(9) is not energetically favorable. Periodic CrNW(9) is energetically more stable than the molecule.

4.3.3 Electronic and Magnetic Properties

Up to now we have investigated the structural, elastic and stability properties of CrNWs. In this subsection, we will deal with the magnetic and electronic properties of them. CrNW(9) in its relaxed geometric structure with 2.84 Ålattice constant is calculated to be metallic as indicated in Fig. 4.6 (a). Conduction of electrons are distributed uniformly in CrNW(9) structure. It can be said by looking at the density of states (DOS) plot that there is a polarization around the Fermi energy. Majority spin states are dominant in these ranges. By looking at the total magnetic moment (which is $2.96\mu_B$), there must appear an excess majority spin states in the system. The magnetic moment distribution on individual atoms are indicated in Fig. 4.6 (b) with the bond lengths of atoms. The magnetic state appears to be ferrimagnetic where nearest neighboring atoms coupled antiferromagnetically with each other. Ferromagnetic coupling occurs when the distance between the atoms are larger than $\sim 2.5\mathring{A}$. The amplitude of
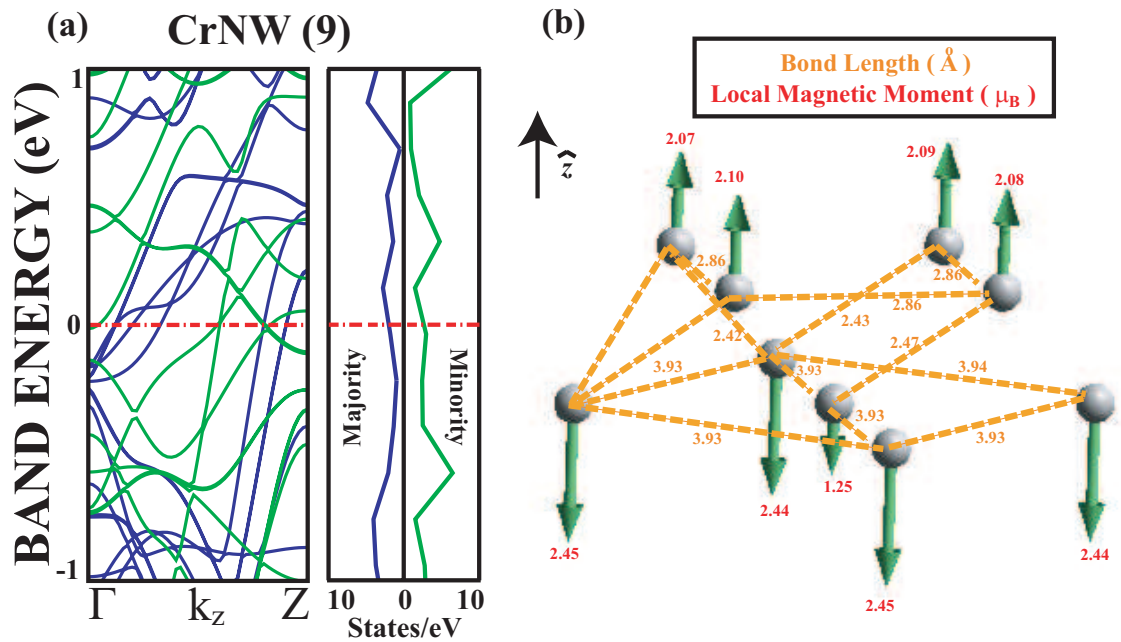
Figure 4.6: Energy band structures of CrNW(9) structure. (a) The zero of energy is set at the Fermi level. Gray and black lines are minority and majority spin bands, respectively. Density of states for minority and majority spin bands are also included. (b) Collinear magnetic moment distribution on the atoms of CrNW(9) unit cell is given. The length and direction of arrows on each atom are proportional with the actual magnetic moments.
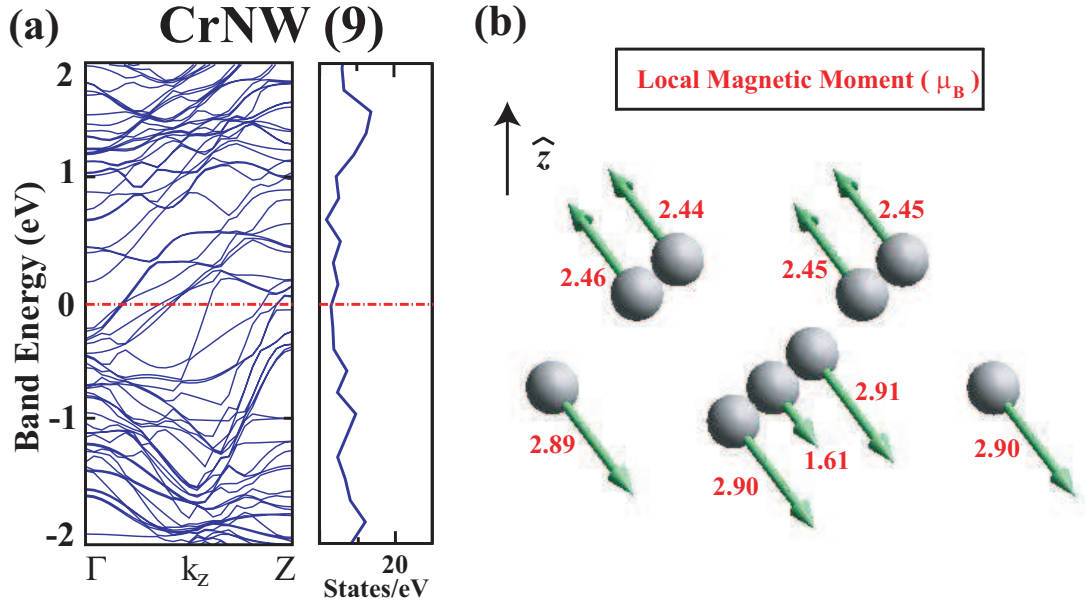
Figure 4.7: Energy band structures of CrNW(9) structure calculated with non-collinear magnetic moment formalism. Spin-orbit coupling effects are also included. (a) The zero of energy is set at the Fermi level. Density of states of the system is indicated. (b) Noncollinear magnetic moment distribution on the atoms of CrNW(9) unit cell is given. The length and direction of arrows on each atom are proportional with the actual magnetic moments.

the magnetic moments on atoms that are coupled antiferromangetically are not the same. Surface atoms generally have higher magnetic moments due to the existence of dangling bonds. The atom which does not have dangling bond is the center atom at the layer which has 5 Cr atoms and magnitude of the magnetic moment is the lowest of all other atoms.

In noncollinear magnetism (NC) calculations, the charge densities are obtained from collinear magnetic calculations and further modified by NC formalism. Initial easy axis of magnetization is taken in [001] direction and further determined in the course of geometric relaxation. The electronic band structure of CrNW(9) is indicated in Fig. 4.7 (a). When the band structure is carefully examined, is is very similar with the band structure calculated by using collinear formalism, but magnetic moment on individual atoms indicated in Fig. 4.7 (b) is
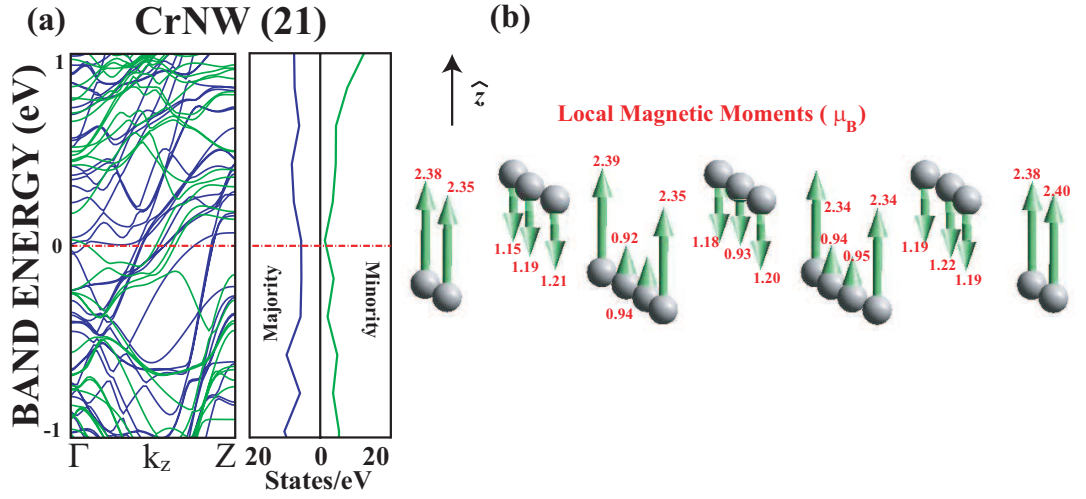
Figure 4.8: Energy band structures of CrNW(21) structure. (a) The zero of energy is set at the Fermi level. Gray and black lines are minority and majority spin bands, respectively. Density of states for minority and majority spin bands are also included. (b) Collinear magnetic moment distribution on the atoms of CrNW(21) unit cell is given. The length and direction of arrows on each atom are proportional with the actual magnetic moments.

tilted from the collinear case with $\theta = 53^o$ and $\phi = 42^o$ in spherical coordinates. From this we can conclude that easy axis of magnetization is lying in the direction of magnetic moments. The cohesive energy of a Cr atom is also increased by 50 meV by including the spin-orbit coupling effects.

The electronic band structure and magnetic moment distribution on individual atoms of CrNW(21) are indicated in Fig . 4.8. From the electronic band structure and DOS, one can easily conclude that CrNW(21) is metallic and there is a majority spin polarization around the Fermi energy level. The conduction of electrons are distributed uniformly over the unit cell. The magnetic state of CrNW(21) is calculated to be ferrimagnetic in which nearest neighbor atoms coupled antiferromagnetically between each other. Longer bond lengths result in ferromagnetic coupling. As observed in CrNW(9), atoms having fewer dangling bonds have smaller magnetic moment amplitude, whereas surface atoms have the highest magnetic moment amplitude among every other Cr atoms in the unit cell. To conclude this subsection, one can say that CrNW(9) and CrNW(21)

are all metallic and there are majority spin polarizations around the Fermi energy. Spin-orbit interaction effects plays an important role in determining the lowest energy magnetic configuration. The magnetic interactions are similar for CrNW(9), CrNW(21) and Cr molecule consisting of 9 atoms explained in previous subsection. Both antiferromagnetic and ferromagnetic couplings occur in the magnetic moment distribution on atoms of CrNW which result in ferrimagnetic magnetic state of CrNWs.

Chapter 5

Conclusions and Future Work

In this thesis, we presented an extensive study of the structural, electronic and magnetic properties of monatomic chains of *3d* transition metal atoms (Sc, Ti, V, Cr, Mn, Fe, Co, Ni as well as Cu and Zn) and Cr nanowires using first-principle plane wave methods. We considered infinite and periodic chains (with linear, dimerized linear, zigzag and dimerized zigzag geometry) and small finite-size chains including 2-7 atoms. Due to the end effects, we found differences between infinite chains and finite ones. Therefore, we believe that the basic understanding of monatomic TM chains have to comprise both infinite and finite structures as done in the present paper.

The infinite, dimerized linear structures have a shallow minimum only for a few TM atoms; planar zigzag and dimerized zigzag structures, however, correspond to a lower binding energy providing stability in this geometry. As for short chains consisting of 4-7 TM atoms, the planar zigzag structure is only a local minimum. The finite chains tend to form clusters if they overcome energy barriers. We found close correlation between the magnetic state and the geometry of the chain structure. In this study, we presented the variation of binding energy as a function of the lattice constant for different structures and the magnetic states. We also revealed the dependence of the electronic and magnetic properties on the atomic structures of chains. We found that the geometric structure influences strongly the electronic and magnetic properties of the chains. For example, infinite linear

V chain becomes half-metallic upon dimerization. Similarly, infinite dimerized linear and metallic Sc chain becomes half-metallic with 100% spin-polarization at the Fermi level upon transformation to zigzag structure. Furthermore, while the infinite linear Mn chain has an antiferromagnetic ground state, with $\mu = \sum \mu_a = 0$, but $|\sum \mu_a^\uparrow| = |\sum \mu_a^\downarrow| = 4.40 \ \mu_B$, it becomes a ferromagnetic metal with $\mu = \sum \mu_a = 4.36 \ \mu_B$ as a result of the structural transformation from linear to dimerized zigzag structure.

Magnetic ordering of finite-size chains becomes more complex and requires a treatment using noncollinear approximation. The structure optimizations carried out using ultra-soft pseudopotentials generally result in the same cohesive energy and magnetic moment in both collinear and noncollinear approximations. However, for specific finite chains the total magnetic moments calculated by using PAW potentials with the same initial magnetic moment distribution differ dramatically from ultra-soft results. Of course, our results which covers much more than 3000 different structure optimizations may not include the lowest energy state, but indicates the importance of noncollinear treatment.

Chromium nanowires with different thicknesses are also investigated in this thesis. The structures studied are Cr nanowire having unitcells consisting of 9 [CrNW(9)] and 21 [CrNW(21)] atoms which are all cut from the bcc bulk crystal of Cr. Both CrNW(9) and CrNW(21) have ferrimagnetic ground states. By doubling the unit cell and making various test (comparison of cohesive energy, total magnetic moment, interlayer atomic distances), we concluded that there is no reconstruction on the surface of Cr nanowires. In addition to these, we also showed that the physical properties of Cr nanowire structures are sensitive to elongation and compression, and hence, these can be engineered as detector in various fields.

To determine the stability of Cr nanowire structures, we have carried out two different methods. In the first case, two molecules consisting of 27 and 32 Cr atoms being a part of the periodic CrNW(9) structure and the stability of them are tested using Moleculer Dynamics (MD) calculations at high temperatures. Three different MD calculations are performed on each molecules. Initially

molecules are heated from 0 K to 900 K, relaxed at 900 K for 0.9 ps and then cooled down to 0 K. The geometric structures of molecules changed slightly due to the fact that they are cut from the relaxed CrNW(9) structure, but geometry did not break down. We believe that if there were any kind of structural instability, it would be initiated and also enhanced within these time steps at high temperatures. Another method we proceed is pulling CrNW(9) structure by placing a vacuum with various widths and reoptimizing the structure. This method is done to compare the energetics of dimerization on CrNW(9). We conclude that dimerized structures have lower cohesive energy per atom which results in less stable structure.

The electronic band structure and local mangetic moment distribution is also examined in this paper. From the results we obtained, one can say that CrNW(9) and CrNW(21) are all metallic and there are majority spin polarizations around the Fermi energy. Spin-orbit interaction effects plays an important role in determining the lowest energy magnetic configuration. The magnetic interactions are similar for CrNW(9) and CrNW(21). Both antiferromagnetic and ferromagnetic couplings occur in the magnetic moment distribution on atoms of CrNW which result in ferrimagnetic magnetic state of Cr nanowires. As a result, Cr nanowires with various thickness are stable, ferrimagnetic metallic structures which may be used in most of the spintronic application, not only in junctions of devices, but also in devices, themselves. Our results indicate also that finite size CrNWs can be utilized as permanet nanomagnets or magnetic molecules.

Bibliography

[1] R.H. Kodama, J. Magnetism and Magnetic Materials **200** (1999) 359-372.

[2] K. Tsukagoshi, B. W. Alphenaar, H. Ago,Nature **401**, 572 (1999).

[3] S. Ciraci, A. Buldum, I. P. Batra, J. Phys. Condens. Matter **13**, 568 (2001).

[4] S. Ciraci, S. Dag, T. Yildirim, O. Gulseren, J. Phys. Condens. Matter **16**, 901 (2004); E. Durgun, D. Cakir, N. Akman, S. Ciraci, Phys. Rev. Lett. **99**, 256806 (2007).

[5] Y.Mokrousov, G. Bihlmayer, S. Blügel, S.Heinze, Phys. Rev. B **75**, 104413 (2007).

[6] C.M. Schneider, J. Kirschner, Handbook of Surface Science(eds K. Horn, M. Scheffler) 511-668 (Elseiver,Amsterdam, 2000).

[7] B.J. van Wees, H. van Houten, C. W. J. Beenakker, J. G. Williamson, L. P. Kouwenhoven, D. varderMarel, C. T. Foxon, Phys Rev. Lett. **60**, 848 (1988).

[8] P. Gambardella, A. Dallmeyer, K. Maiti, M.C. Malagoli, W. Eberhardt, K.Kern, C. Carbone,Nature **416**, 301 (2002).

[9] N. Agrait, A.L. Yeyati, J.M. van Ruitenbeek,Phys. Rep 377, 81(2003).

[10] A.I. Yanson, G. Rubio-Bollinger, H.E. van den Brom, N. Agrait, J.M. van Ruitenbeek,Nature **395**, 783 (1998).

[11] H. Ohnishi, Y.Kondo, K. Takayanagi,Nature **395**, 780 (1998).

[12] M.R. Sorensen, M.Brandbyge, K.W. Jacobsen,Phys Rev. B **57**, 3283 (1998).

[13] H. Hakkinen, R.N. Barnett, U.Landman, J. Phys.Chem B. **103**, 8814 (1999).

[14] D.Sánchez-Portal, E. Artacho, J. Junquera, P. Ordejón, A. Garcia, J. M. Soler, Phys Rev. Lett. **83**, 3884 (1999).

[15] J.A. Torres, E. Tosatti, A.D. Corso, F. Ercolessi, J.J. Kohanoff, F.D. Di Tolla, and J.M. Soler, Surf. Sci. 426, L441 (1999).

[16] M. Okamoto, K. Takayanagi,Phys Rev. B **60**, 7808 (1999).

[17] V. Rodrigues, T. Fuhrer, D. Ugarte,Phys. Rev. Lett. **85**, 4124 (2000).

[18] P. Sen, S. Ciraci, A. Buldum, I. P. Batra, Phys. Rev. B **64**, 195420 (2001).

[19] P. Sen, O. Gulseren, T. Yildirim, I. P. Batra, S. Ciraci, Phys. Rev. B **65**, 235433 (2002).

[20] S. Tongay, R. T. Senger, S. Dag, S. Ciraci, Phys. Rev. Lett. **93**, 136404 (2004).

[21] O. Gurlu, H. J. W. Zandvliet, B. Poelsema, S. Dag, S. Ciraci, Pjys. Rev. B **70**, 085312 (2004).

[22] J. Dorantes-Davila, G.M. Pastor, Phys Rev. Lett. **81**, 208 (1998).

[23] A. Delin, E. Tosatti, J. Phys.: Condens. Matter **16** 8061-8074 (2004).

[24] A. Bala, T. Nautiyal, K.S. Kim, Phys Rev. B **74**, 174429 (2006).

[25] Y. Mokrousov, G. Bihlmayer, S. Heinze, S. Blügel, Phys Rev. Lett. **96**, 147201 (2006).

[26] A. Delin, E. Tosatti, Phys Rev. B **68**, 144434 (2003).

[27] M. Wierzbowska, A. Delin, E. Tosatti, Phys Rev. B **72**, 035439 (2005).

[28] S. A. Wolf, D. D. Awschalom, R. A. Buhrman, J. M.Daughton, S. von Molnár, M. L. Roukes, A. Y. Chtchelkanova,and D. M. Treger, Science **294**, 1488 (2001).

[29] E. Durgun, R. T. Senger, H. Mehrez, H. Sevincli, S. Ciraci, J.Chem. Phys. **125**, 121102 (2006).

[30] H. Kachkachi, J. Magnetism and Magnetic Materials **316** (2007) 248-254.

[31] V.L. Moruzzi,Phys Rev. Lett. **57**,2211 (1986).

[32] M. Luban, J. Magnetism and Magnetic Materials **272-276** (2004) e635-e641.

[33] V. Heine, J.H. Samson, C.M.M. Nex, J.Phys.F. Metal Phys. **11** (1981) 2645-2662.

[34] P. Gambardella, J. Phys.: Condens. Matter **15** (2003) 2533-2546.

[35] M.B. Knickelbein, Phys Rev. B **70**, 014424 (2004).

[36] R.F. Wallis, Phys Rev. **105**, 540 (1957).

[37] J. Schnack, arXiv:cond-mat/0501625_v1

[38] M. C. Payne, M. P. Teter, D. C. Allen, T. A. Arias, and J. D. Joannopoulos, Rev. Mod. Phys. **64**, 1045 (1992).

[39] J. Perdeq, R. G. Parr, M. Levy, J. L. Balduz, Phys. Rev. Lett. **49**, 1691, (1982).

[40] H.J. Monkhorst and J.D. Pack, Phys. Rev. B **13**, 5188, (1976).

[41] D. Hobbs, G. Kresse, J.Hafner, Phys. Rev. B **62**, 11556 (2000).

[42] Ph. Kurz, F. Förster, L. Nordström, G. Bihlmayer, S. Blügel, Phys. Rev. B **69**, 024415, (2004).

[43] J. Anton, B. Fricke, E. Engel, Phys. Rev. A **69**, 012505, (2004).

[44] J. Kübler, K-H Höck, J. Sticht, A. R. Williams,J. Phys. F: Met. Phys. **18**, 469-483 (1988).

[45] T. Oda, A. Pasquarello, R. Car, Phys. Rev. Lett. **80**, 3622, (1998).

[46] S. Sharma, J.K. Dewhurst, C. Ambrosch-Draxl, S. Kurth, N. Helbig, S. Pittalis, S. Shallcross, L. Nordström, E. K. U. Gross, Phys. Rev. Lett. **98**, 196405, (2007).

[47] Numerical computations have been carried out by using VASP software: G. Kresse, J. Hafner, Phys Rev. B **47**, R558 (1993); G. Kresse, J. Furthmuller, Phys Rev. B **54**, 11169 (1996).

[48] W. Kohn and L. J. Sham, Phys. Rev. 140, A1133 (1965); P. Hohenberg and W. Kohn, Phys. Rev. B 76, 6062 (1964).

[49] D. Vanderbilt, Phys. Rev. B **41**, R7892 (1990).

[50] G. Kresse, and D. Joubert, Phys. Rev. B **59**, 1758 (1999).

[51] J. P. Perdew, J. A. Chevary, S. H. Vosko, K. A. Jackson, M. R. Pederson, D. J. Singh, and C. Fiolhais, Phys. Rev. B **46**, 6671 (1992).

[52] M. Methfessel and A. T. Paxton, Phys. Rev. B **40**, 3616 1989.

[53] A. Sommerfeld, H. Bethe, Handbuch der Physik, Springer, Berlin, 1933.

[54] J. Friedel; The Physics of Metals; Ziman, J. M., Ed.; Cambridge University Press: New York, 1969. D. G. Pettifor, Solid State Physics; Ehrenreich, H., Turnbull, D., Eds.; Academic Press: New York, 1987; Vol. 40, p 43.

[55] Introduction to Solid State Physics, C. Kittel, John Willey and Sons, New York, Chichester, Brisbane, Toronto, Singapore,7th Ed., 1996).

[56] J. C. Tung, G. Y. Guo, Phys. Rev. B **76**, 094413, (2007).

[57] S. Nosé, Mol. Phys. **52**, 255–268, (1984).